Australian Government
Department of Defence
Defence Science and
Technology Organisation

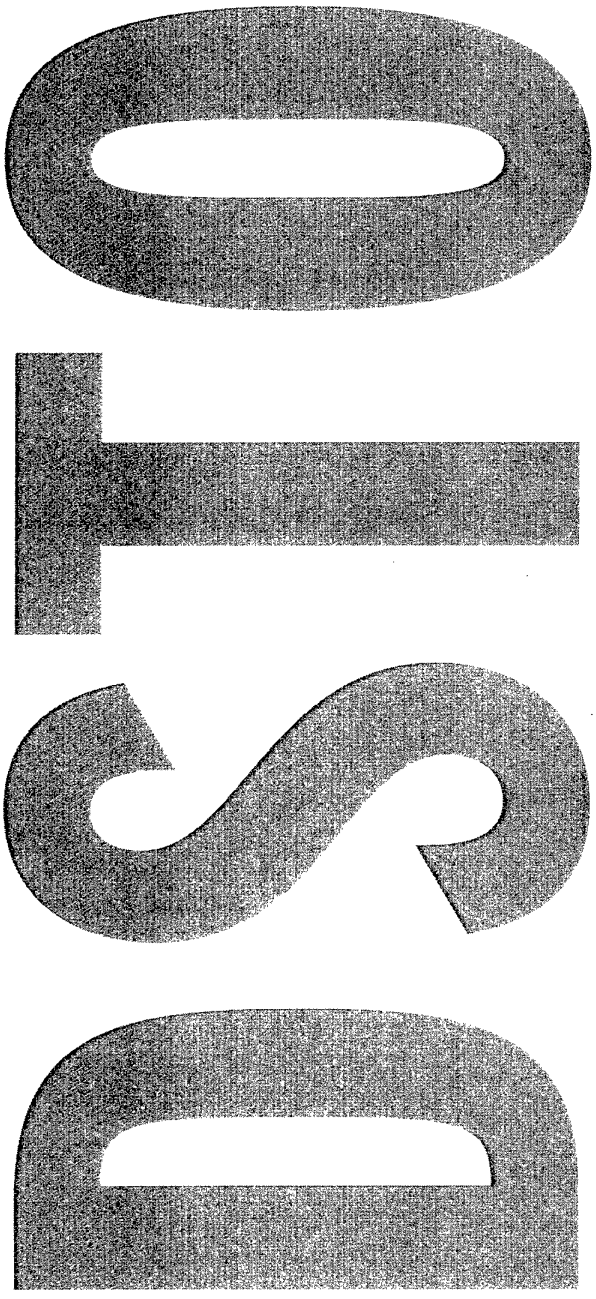

Steady-State Evaluation of 'Two-Equation' RANS (Reynolds-averaged Navier-Stokes) Turbulence Models for High-Reynolds Number Hydrodynamic Flow Simulations

Nicholas J. Mulvany, Li Chen, Jiyuan Y. Tu and Brendon Anderson

DSTO-TR-1564

Australian Government
Department of Defence
Defence Science and
Technology Organisation

Steady-State Evaluation of 'Two-Equation' RANS (Reynolds-averaged Navier-Stokes) Turbulence Models for High-Reynolds Number Hydrodynamic Flow Simulations

Nicholas J. Mulvany, Li Chen, Jiyuan Y. Tu and Brendon Anderson

Maritime Platforms Division
Platform Sciences Laboratory

DSTO-TR-1564

ABSTRACT

This report presents an evaluation of the steady-state capability of the turbulence models available in the commercial CFD code FLUENT 6.0, for their application to the simulation of hydrofoil turbulent boundary layer separation at high-Reynolds numbers. Four widely applied two-equation RANS turbulence models were qualitatively and quantitatively assessed through comparison with high-quality experimental data at Reynolds numbers of 8.284´106 and 1.657´107. The turbulence models evaluated were the Standard k-e model, the Realisable k-e model, the Standard k-w model and the Shear-Stress-Transport (SST) k-w model. It was concluded that the Realisable k-e turbulence model used with enhanced wall functions and near-wall modelling techniques, consistently provided superior performance in predicting the hydrofoil's performance parameters and flow characteristics.

RELEASE LIMITATION

Approved for public release

Published by

DSTO Platform Sciences Laboratory
506 Lorimer St.
Fishermans Bend, Victoria 3207 Australia

Telephone: (03) 9626 7000
Fax: (03) 9626 7999

AR-013-055
March 2004

APPROVED FOR PUBLIC RELEASE

Steady-State Evaluation of 'Two-Equation' RANS (Reynolds-averaged Navier-Stokes) Turbulence Models for High-Reynolds Number Hydrodynamic Flow Simulations

Executive Summary

Hydrodynamic flows of interest to designers of large surface and sub-surface marine vessels and their propulsors are typically characterised by high-Reynolds numbers and usually some form of flow unsteadiness. To numerically model such flows poses significant challenges to the current range of 'two-equation' RANS (Reynolds-Averaged Navier-Stokes) turbulence models.

In an effort to determine the most accurate turbulence model for high-Reynolds number hydrodynamic flows, an evaluation of the steady-state capability of the turbulence models available in the commercial CFD code FLUENT 6.0 has been undertaken. This evaluation is limited to applications to the simulation of hydrofoil turbulent boundary layer separation at high-Reynolds numbers.

Four widely applied two-equation RANS turbulence models were qualitatively and quantitatively assessed through comparison with high-quality experimental data at Reynolds numbers of 8.284×10^6 and 1.657×10^7. In this preliminary investigation, the turbulence models evaluated were the Standard k-ε model, the Realisable k-ε model, the Standard k-ω model and the relatively new Shear-Stress-Transport (SST) k-ω model.

It was concluded that the Realisable k-ε turbulence model used in conjunction with enhanced wall functions and near-wall modelling techniques, consistently provided superior performance in predicting the hydrofoil's performance parameters and flow characteristics. This turbulence model and wall treatment accurately predicted the pressure coefficient distribution, the lift and drag coefficients, the pressure surface boundary layer characteristics, the separation of the suction surface boundary layer and the flow features in the near wake region.

Authors

Nicholas J. Mulvany
Vacation Student - Maritime Platforms Division

Nicholas Mulvany graduated from RMIT University with a B.Eng. (Mech) (Hons) in 2002. Nicholas specialised in thermodynamics, fluid mechanics and computational engineering. He joined Aeronautical and Maritime Research Laboratory in 2002 as a vacation scholar within the Undersea Platform Hydrodynamics group of the Maritime Platforms Division.

Li Chen
Maritime Platforms Division

Li Chen is a Research Scientist (S&T5) in MPD Melbourne. She graduated with a Bachelor of Engineering (First Class Honours, major in HVAC) in 1982 from University of ChongQing, China and received her PhD in 1997 from University of New South Wales. She Joined DSTO in 1999 after working in research and academic positions. In MPD her work has mainly involved in the reduction of flow-induced acoustic from submarine and modelling turbulent flows and hydro-acoustic.

JiYuan Tu
School of Mech. & Manu. Eng. RMIT University

JiYuan Tu is an associate professor in CFD in the Department of Mechanical Engineering, RMIT University. Dr Jiyuan Tu graduated from the Department of Mechanical Engineering, Northeastern University, China, with B. Eng and M. Eng. Sc. degrees in 1982 and 1984 respectively. Dr Tu worked then as a lecturer in Department of Physics, Fudan University, China, between 1984 and 1989. He received his Ph.D. in Computational Fluid Dynamics (CFD) from Department of Mechanics, The Royal Institute of Technology, Sweden in 1992. Professor Tu has received many awards, prizes and prestigious fellowships in recognition of his contributions to the field, including Japan Society for the Promotion of Science (JSPS) fellowship, Korea Science and Engineering Foundation (KOSEF) fellowship, US-Australia, and Australia-Europe Exchange Fellowships from Australian Academy of Science (AAS). He has extensive research experience and expertise in computational fluid dynamics and computational heat transfer with particular interest in turbulence modelling and flow simulation in various complex geometries.

Brendon Anderson
Maritime Platforms Division

Brendon Anderson is a Senior Research Scientist (S&T 6) in the Maritime Platforms Division. Brendon Anderson graduated from Monash University with a B.Sc. (Mathematics) in 1989. In 1990, he began working with DSTO in the Underwater Weapons and Countermeasure Systems Division, now the Maritime Operations Division, before joining the Maritime Platforms Division in 1998. In 1999 he completed a M. Eng. Sc. degree with the University of Tasmania for his work on the determination of hydrodynamic coefficients using a planar motion mechanism. In 1999, Mr. Anderson was awarded a Defence Science Fellowship to study Underwater Vehicle Technologies at the United States Naval Undersea Warfare Center for twelve months. On return from his posting in 2000 he was appointed the head of MPD's hydrodynamics group. His current work includes hydrodynamic modelling of submarines for the Australian Navy.

Contents

List of Figures

List of Tables

1. Introduction

Hydrodynamic flows of interest to designers of large surface and sub-surface marine vessels and their propulsors are typically very complex. The length scales and the relative flow velocities in both the free-stream and induced fields of these vessels produce flows characterised by very high Reynolds numbers. Together they pose the greatest challenge to both the experimental and theoretic researches in modern fluid dynamics. Such flows can typically exceed Reynolds numbers of 10^7 [1], yet can reach magnitudes of 10^9 and 10^{10} [2]. Secondly, these flows exhibit of high unsteadiness or time-dependent phenomena, such as the shedding of vortices from propeller blades, control surfaces and other submerged appendage. Thirdly, with the occurrence of cavitation these flows can also be multiphase.

The expectations placed upon solution methodology, computational software and computer hardware to simulate these hydrodynamic flows using numerical methods are immense. With the emergence of parallel computing and its provision of reduced global memory and run-times through multiple processors, numerical solutions are becoming more achievable for increasingly complex problems [3]. Parts of larger three-dimensional flow problem that were previously simulated individually are now being simulated as complete configurations, such as full submarine geometries comprising hull, sail, stern appendage, propeller and moving control surfaces for both steady and unsteady flow scenarios [3].

Given that both Direct Numerical Simulation (DNS) and Large-Eddy Simulation (LES) are still untenable approaches in practical flows, the modelling of most practically relevant turbulent flows, such as most hydrodynamic flows, is widely based upon the solution of Reynolds-Averaged NS (RANS) equations. As a result, accurate modelling of Reynolds stresses becomes crucial. There are various turbulence modelling approaches. Questions remain about whether or not the available turbulence models predict the correct flow physics and which turbulence models are best suited to what type of flows. It is agreed [3] that it is both naive and dangerous to assume the validity of a turbulence model over a wide range of flows. It is also agreed that unique modification or refinement of existing turbulence models for specific flow applications may provide improved performance. Many evaluations of two-equation RANS turbulence models documented in the literature have been undertaken in order to identify the most suitable model for the particular flow of interest.

Speziale et. al. [4] applied a variety of two-equation (k-ε and k-ω variants) models and their k-τ model to near-wall turbulent flows. They concluded that due to the excessively high levels of destruction-dissipation and turbulence viscosity near the wall, the predictions of the k-ε models tested were severely compromised. As far as the k-ω model of Wilcox et. al. [5, 6] was concerned, this model had the same constraints as the k-ε models, yet returned excessive turbulent kinetic energy near the wall. However, for many applications, the k-ω model provided adequate prediction of the skin friction

at the wall and the turbulence statistics away from the wall. Based on the numerical tests of Speziale et. al. [4], their k-τ turbulence model seemed to have improved predictions within the turbulent boundary layer.

Lien & Leshziner [7] examined both a non-linear eddy-viscosity model and a second-moment closure model by applying them to 2D separated flow from a high-lift airfoil. They concluded that the second-moment closure produced superior predictions relative to both the non-linear eddy-viscosity model and the realisable Reynolds stress algebraic model of Shih et. al. [8]. The second-moment closure model had the inherent ability of representing the interaction between streamline curvature and turbulence anisotropy, and the effect of anisotropy on shear stress. Nevertheless, the second-moment model failed to predict the onset of separation at the correct angle of attack. The failure was attributed to the excessively high levels of shear stress near the wall, preventing separation.

Pajayakrit & Kind [9] evaluated four turbulence models for predicting the development of plane and curved wall jet flows. The models evaluated were the Baldwin & Lomax [10] algebraic model, the Dash et. al. [11] k-ε model, the Wilcox [5] k-ω and the Wilcox [6] multi-scale model. Without any modification, all models demonstrated significant deficiencies, although the Dash et. al. [9] k-ε model performed reasonably well on an overall sense, particularly for the curved wall jet flow. Fine tunning of the Wilcox [5,6] models was undertaken by adjusting the model constants, however, improvement was achieved by the modified k-ω model only.

Unlike the work presented by Speziale et. al. [4], Lien & Leshziner [7] and Pajayakrit & Kind [9], Kim et. al. [12] evaluated three widely applied and economic turbulence models using a practical problem; the hull form design of a very large crude-oil carrier. The turbulence models evaluated were the Standard k-ε model, the RNG k-ε model and the Realisable k-ε model. Emphasis was placed on their ability to accurately predict the nominal wake distribution at the propeller plane, a region of strong bilge vortices and complex flow behaviour, as flow information within this region is vital for propeller design. It was determined that the Realisable k-ε turbulence model accurately predicted the strength and location of the bilge vortex, however, both the Standard k-ε and RNG k-ε turbulence models failed to predict this flow feature.

This report is not intended as an authoritative reference for turbulence model applications for all hydrodynamic flow simulations, nor have we aimed to discuss the strengths and weaknesses of the turbulence models at a detailed level. Rather, like the work presented by Kim et. al. [12], it report is intended as a guide to researchers and designers who are working on a similar hydrodynamic problem.

The hydrodynamic problem of interest in this report is the numerical simulation of the turbulent hydrofoil flow at high Reynolds numbers, where the boundary layer on the suction surface is subjected to a large adverse pressure gradient. This category of turbulent flow poses major modelling challenges for the predictive capabilities of any

turbulence model. Such turbulent boundary layer separation occurs at the trailing edge of hydrofoils operating at high Reynolds numbers, resulting in the formation of unsteady oscillating wakes. Under certain conditions the vortex-shedding period of the wake may become coincident with the resonant frequency of the hydrofoil or parts of it, resulting in the emission of a high-level tonal noise. Such an emission from lifting surfaces associated with naval vessels is highly undesirable, as this noise is a dominant source of information for underwater detection systems. This preliminary study evaluates the steady-state capability of several two-equation RANS turbulence models using the commercial CFD code FLUENT 6.0. The four turbulence models evaluated are the Standard k-ε, the Realisable k-ε, the Standard k-ω and the relatively new Shear-Stress-Transport (SST) k-ω, as detailed in the literature [13].

Also, in an effort to provide researchers with a guide to the application of wall functions in such a flow scenario, three different wall treatments are investigated with respect to their suitability. These include two different wall functions, the standard and non-equilibrium variants, and enhanced wall treatment employing near-wall modelling techniques.

The developed CFD model is based on the characteristics and parameters of the recent experimental research into high-Reynolds number hydrofoil flow, undertaken by Bourgoyne et. al. [1,14 and 15], allowing direct comparison to high-quality experimental data.

2. Problem Overview

The main objective of the experimental research conducted by Bourgoyne et. al. [1, 14 and 15] was to identify and document the dominant flow features in the trailing edge region of a hydrofoil operating at chord-based Reynolds numbers approaching 10^8. In addition this research has provided a database of high-quality experimental data for the development, refinement and validation of turbulence models for high-Reynolds number applications.

The research was conducted in the William B. Morgan Large Cavitation Channel (LCC) in Memphis, USA. The test hydrofoil was fully two-dimensional, spanning the test section (3.05m), with a chord length (C) of 2.134m. The cross-section profile was representative of a generic naval propeller of moderate thickness (t) and camber (f), utilising a NACA-16 airfoil profile ($t/C = 0.08$, $f/C = 0.032$) with two modifications.

The first modification was that the pressure surface of the hydrofoil was flat beyond 28% chord length continuing to the trailing edge. The second modification was that near 97% chord length, the suction surface steeply terminated at the trailing edge at an angle of 44^0 to the flat pressure surface, a characteristic typical of anti-singing trailing edges. A detailed diagram of the hydrofoil geometry is illustrated in Figure 1 and the anti-singing trailing edge geometry is detailed in the literature [1].

Experiments were conducted at flow velocities of 0.5m/s to 18.3m/s, corresponding to chord-based Reynolds numbers of 1.4×10^6 to 6×10^7. The hydrofoil was aligned with the flow (i.e. zero angle of attack) and its mounting method within the water tunnel produced good span-wise two-dimensional flow [1]. Laser-Doppler-Velocimetry (LDV) and Particle-Imaging-Velocimetry (PIV) measurement techniques were used to determine mean flow velocities and turbulence statistics from the separating boundary layer flow near the hydrofoil's trailing edge. Static pressure measurements on the surface of the hydrofoil were made using seventeen suction-side and thirteen pressure-side taps.

The mean flow velocities at 2500 co-ordinate positions within the trailing edge region were measured using the LDV system. A nominal sampling period of 36 seconds per co-ordinate was used, with the number of samples varying between 500 and 12000. The vortex shedding period of the hydrofoil was theoretically calculated to be 60 ms at a flow speed of 3 m/s and 10 ms at 18.3m/s. Therefore, the sampling period was equal to between 600 to 3600 shedding periods, allowing accurate resolution of the mean properties within the unsteady flow. The LDV system was determined to have a maximum calibration bias range in the normalised mean velocities of ±0.02 at 3m/s to ±0.006 at 18.3m/s [1]. The positioning error of the LDV system was assessed as ±0.1mm, equivalent to ±0.0047% of the chord [1].

Two main conclusions were drawn from the experimental testing. Firstly, the hydrofoil's near wake flow features appeared to be Reynolds number dependent and, secondly, the observation of Reynolds number dependency is consistent with suction-side boundary layer separation occurring closer to the trailing edge with increasing Reynolds number.

Although the application of numerical methods to hydrodynamic lifting surface flow is widespread in the literature [16, 17, 18 & 19] and has greatly matured, there are specific challenges posed to numerically modelling the experimental testing conducted by Bourgoyne et. al. [1, 14 & 15]. Firstly, the experimental testing was conducted at a Reynolds numbers well above the range at which the turbulence models were validated. Secondly, the numerical model must accurately predict the separation of the turbulent boundary layers from both the pressure and suction surfaces at the trailing edge. Separation itself is a highly complex physical phenomenon, and it also introduces mesh issues in numerical modelling. Thirdly and most importantly for hydroacoustic research, the numerical model must also be able to correctly resolve the shedding of vortices and the formation of an oscillating wake.

Of particular importance to this preliminary steady-state analysis is boundary layer separation. In this flow configuration with a slender and streamlined body, the numerical modelling of turbulent boundary layer separation is more challenging due to its Reynolds number dependency. It has been shown experimentally by both Baubeau & Latorre [17] and Bourgoyne et. al. [1] that at a constant angle of attack, a turbulent boundary layer resists separation further along the surface of a hydrofoil, separating closer to the trailing edge with increasing Reynolds number.

Correct modelling of turbulent boundary layer separation is crucial for the accurate prediction of the coefficients of lift and drag. Incorrect prediction of the separation location can lead to errors in the magnitude of the low-pressure recirculation bubble at the trailing edge, hence over- or under-prediction of the pressure drag of the hydrofoil.

As in this application the pressure surface of the hydrofoil is flat, separation of the pressure surface boundary layer at the trailing edge tip is inevitable. Therefore emphasis is placed upon the prediction of the suction surface boundary layer separation from the anti-singing trailing edge.

3. Theory

3.1 Governing Equations

The governing equations for the turbulent incompressible flow encountered in this research are the steady-state Reynolds-averaged Navier-Stokes (RANS) equations for the conservation of mass and momentum. In the literature [13] they are presented in the following forms:

Continuity:

$$\frac{\partial}{\partial x_i}\left(\overline{\rho u_i}\right) = 0 \tag{1}$$

Momentum:

$$\frac{\partial}{\partial x_j}\left(\overline{\rho u_i u_j}\right) = -\frac{\partial \bar{p}}{\partial x_i} + \frac{\partial}{\partial x_j}\left[\mu\left(\frac{\partial \bar{u}_i}{\partial x_j} + \frac{\partial \bar{u}_j}{\partial x_i} - \frac{2}{3}\delta_{ij}\frac{\partial \bar{u}_l}{\partial x_l}\right)\right] + \frac{\partial}{\partial x_j}\left(-\overline{\rho u_i' u_j'}\right) \tag{2}$$

In Equations (1) and (2), $\bar{\rho}$ is mean density, $\bar{p}$ is mean pressure, μ is the molecular viscosity and $-\overline{\rho u_i' u_j'}$ is the Reynolds stresses. To correctly account for turbulence, Reynolds stresses are modelled in order to achieve closure of Equation (2). The method of modelling employed utilises the Boussinesq hypothesis to relate the Reynolds stresses to the mean velocity gradients within the flow. Therefore the Reynolds stresses are given by:

$$-\overline{\rho u_i' u_j'} = \mu_t\left(\frac{\partial \bar{u}_i}{\partial x_j} + \frac{\partial \bar{u}_j}{\partial x_i}\right) - \frac{2}{3}\left(\rho k + \mu_t \frac{\partial \bar{u}_i}{\partial x_i}\right)\delta_{ij} \tag{3}$$

In Equation (3), μ_t is the turbulent (or eddy) viscosity and k is the turbulent kinetic energy. For two-equation turbulence models such as the k-ε and k-ω variants, the turbulent viscosity is computed through the solution of two additional transport equations for the turbulent kinetic energy, and either the turbulence dissipation rate, ε, or the specific dissipation rate, ω.

3.2 Two-Equation Turbulence Models

3.2.1 Standard k-ε

The Standard k-ε turbulence model is presently the most widely applied turbulence model to practical engineering flows as it is robust, economical and provides reasonable accuracy for a wide range of flows. The transport equation for k is physically correct, however the transport equation for ε is heavily modelled [13]. The modelled transport equations for k and ε, for steady-state and incompressible flow, are given in the literature [13] as:

$$\frac{\partial}{\partial x_i}\left(\rho k \bar{u}_i\right) = \frac{\partial}{\partial x_j}\left[\left(\mu + \frac{\mu_t}{\sigma_k}\right)\frac{\partial \varepsilon}{\partial x_j}\right] + G_k - Y_k \tag{4}$$

$$\frac{\partial}{\partial x_i}\left(\rho \varepsilon \bar{u}_i\right) = \frac{\partial}{\partial x_j}\left[\left(\mu + \frac{\mu_t}{\sigma_\varepsilon}\right)\frac{\partial \varepsilon}{\partial x_j}\right] + G_\varepsilon - Y_\varepsilon \tag{5}$$

In Equations (4) and (5), σ_k and σ_ε are the turbulent Prandtl numbers for k and ε respectively. The production of turbulence kinetic energy, G_k, is approximated in a manner consistent with the Boussinesq hypothesis by:

$$G_k = \mu_t S^2 \tag{6}$$

S is the modulus of the mean rate-of-strain tensor, defined by:

$$S \equiv \sqrt{2 S_{ij} S_{ij}}$$

$$S_{ij} = \frac{1}{2}\left(\frac{\partial \bar{u}_j}{\partial x_i} + \frac{\partial \bar{u}_i}{\partial x_j}\right)$$

The dissipation of this turbulence kinetic energy, Y_k, is defined by:

$$Y_k = \rho \varepsilon \tag{7}$$

The production and dissipation of ε, G_ε and Y_ε respectively, are defined as:

$$G_\varepsilon = C_{1\varepsilon}\frac{\varepsilon}{k}\left(G_k\right) \tag{8}$$

$$Y_\varepsilon = C_{2\varepsilon}\rho\frac{\varepsilon^2}{k} \tag{9}$$

In Equations (8) and (9), $C_{1\varepsilon}$ and $C_{2\varepsilon}$ are constants. The turbulent viscosity is computed through a formulation of k and ε, given as:

$$\mu_t = \rho C_\mu \frac{k^2}{\varepsilon} \tag{10}$$

In Equation (10), C_μ is a constant, and this constant and the remaining constants applied in the Standard k-ε turbulence model are equal to:

$$C_{1\varepsilon} = 1.44,\ C_{2\varepsilon} = 1.92,\ C_\mu = 0.09,\ \sigma_k = 1.0,\ \sigma_\varepsilon = 1.3$$

3.2.2 Realisable k-ε

The Realisable k-ε turbulence model differs from the Standard k-ε model in two important ways. Firstly it contains a new formulation for the turbulent viscosity, and secondly, a new transport equation for ε has been derived from an exact equation for the transport of the mean-square vorticity function [13].

In the Realisable k-ε turbulence model, the transport equation for k is identical to that of the Standard k-ε model (Equation (4)). However, the production and diffusion terms in the transport equation for ε differ slightly and are defined as:

$$G_\varepsilon = \rho C_1 S\varepsilon \tag{11}$$

$$Y_\varepsilon = \rho C_2 \frac{\varepsilon^2}{k + \sqrt{\nu\varepsilon}} \tag{12}$$

In Equations (11) and (12), C_2 is a constant, while C_1 is defined as:

$$C_1 = \max\left[0.43, \frac{\eta}{\eta + 5}\right]$$

$$\eta = S\frac{k}{\varepsilon}$$

Similarly to the Standard k-ε turbulence model, the turbulent viscosity is computed using Equation (10), however, C_μ is no longer a constant. C_μ is calculated using the following equations:

$$C_\mu = \frac{1}{A_0 + A_s \frac{kU^*}{\varepsilon}} \tag{13}$$

Where:

$$U^* \equiv \sqrt{S_{ij}S_{ij} + \tilde{\Omega}_{ij}\tilde{\Omega}_{ij}}\ ,\ \ \tilde{\Omega}_{ij} = \frac{1}{2}\left(\frac{\partial \bar{u}_i}{\partial x_j} - \frac{\partial \bar{u}_j}{\partial x_i}\right)$$

In Equation (13), A_0 is a constant and the remaining variable, A_S, is calculated using the following:

$$A_s = \sqrt{6}\cos\phi$$

Where:

$$\phi = \frac{1}{3}\cos^{-1}\left(\sqrt{6}W\right),\ W = \frac{S_{ij}S_{jk}S_{ki}}{\tilde{S}^3},\ \tilde{S} = \sqrt{S_{ij}S_{ij}}$$

The constants applied in the Realisable k-ε turbulence model are equal to:

$$\sigma_k = 1.0,\ \sigma_\varepsilon = 1.2,\ C_2 = 1.9,\ A_0 = 4.04$$

3.2.3 Standard k-ω

The Standard k-ω turbulence model incorporates modifications for low-Reynolds number effects and shear flow spreading. The shear flow spreading rates are in close agreement with measurements for far wakes, mixing layers, and plane, round, and radial jets, and is thus applicable to wall-bounded and free shear flows [13].

The modelled transport equation for k in the Standard k-ω turbulence model is very similar to that of the k-ε based models. The production of turbulence kinetic energy is defined identically to that of the k-ε models (Equation (6)), however the Standard k-ω model has a different formulation for the diffusion of k, defined as:

$$Y_k = \rho\beta^*_\infty f_{\beta^*} k\omega \tag{14}$$

Where β^*_∞ is a constant and:

$$f_{\beta^*} = \begin{cases} 1, & \chi_k \le 0 \\ \left[\dfrac{1+680\chi_k^2}{1+400\chi_k^2}\right], & \chi_k > 0 \end{cases}$$

$$\chi_k \equiv \frac{1}{\omega^3}\frac{\partial k}{\partial x_j}\frac{\partial \omega}{\partial x_j}$$

With replacement of ε for ω in Equation (5), the transport equation for ω in the Standard k-ω model is created from that of ε in the k-ε based models. However, the production and diffusion terms of ω are significantly different to those of ε. The production and diffusion of ω in the high-Reynolds number form of the Standard k-ω model are defined respectively as:

$$G_\omega = \frac{\omega}{k}G_k \tag{15}$$

$$Y_\omega = \rho\beta_i f_\beta \omega^2 \tag{16}$$

Where β_i is a constant and:

$$f_\beta = \frac{1+70\chi_\omega}{1+80\chi_\omega}$$

$$\chi_\omega = \left|\frac{\Omega_{ij}\Omega_{jk}S_{ij}}{\left(\beta_\infty^*\omega\right)^3}\right|$$

Again, another deviation of the Standard k-ω from the previous turbulence models is the computation of the turbulent viscosity. For the high-Reynolds number form of the Standard k-ω model, the turbulent viscosity is calculated using:

$$\mu_t = \frac{\rho k}{\omega} \tag{17}$$

The constants applied in the high-Reynolds number form of the Standard k-ω turbulence model are equal to:

$$\sigma_k = 2.0,\ \sigma_\omega = 2.0,\ \beta_\infty^* = 0.09,\ \beta_i = 0.072$$

3.2.4 Shear-Stress-Transport (SST) k-ω

The SST k-ω turbulence model is a conglomeration of the robust and accurate formulation of the Standard k-ω model in the near-wall region, with the Standard k-ε in the far field. The SST k-ω is more accurate and reliable for a wider class of flows than the Standard k-ω, including adverse pressure gradient flows [13].

In the SST k-ω turbulence model, the modelled transport equation for k is identical to that of the Standard k-ω model, however, the transport equation for ω differs slightly with the inclusion of a cross-diffusion term, D_ω.

The production of k in the SST k-ω model is defined in the same manner as per the Standard k-ω model, hence the k-ε type models, by Equation (6). However, variations exist in the production of ω with comparison to the Standard k-ω model. The production of ω is given by:

$$G_\omega = \frac{\alpha_\infty}{\nu_t} G_k \tag{18}$$

Where:

$$\alpha_\infty = F_1 \alpha_{\infty,1} + (1 - F_1)\alpha_{\infty,2}$$

$$\alpha_{\infty,1} = \frac{\beta_{i,1}}{\beta^*_\infty} - \frac{\kappa^2}{\sigma_{\omega,1}\sqrt{\beta^*_\infty}}$$

$$\alpha_{\infty,2} = \frac{\beta_{i,2}}{\beta^*_\infty} - \frac{\kappa^2}{\sigma_{\omega,2}\sqrt{\beta^*_\infty}}$$

The dissipation of the k and ω are defined differently to the Standard k-ω model by the following respectively:

$$Y_k = \rho\beta^* k\omega \tag{19}$$

$$Y_\omega = \rho\beta_i \omega^2 \tag{20}$$

Where:

$$\beta_i = F_1\beta_{i,1} + (1 - F_1)\beta_{i,2} \tag{21}$$

In Equation (21), $\beta_{i,1}$ and $\beta_{i,2}$ are constants while the F_1 is determined from the following:

$$F_1 = \tanh\left(\Phi_1^4\right)$$

$$\Phi_1 = \min\left[\max\left(\frac{\sqrt{k}}{0.09\omega y}, \frac{500\mu}{\rho y^2 \omega}\right), \frac{4\rho k}{\sigma_{\omega,2} D_\omega^+ y^2}\right]$$

$$D_\omega^+ = \max\left[2\rho \frac{1}{\sigma_{\omega,2}} \frac{1}{\omega} \frac{\partial k}{\partial x_j} \frac{\partial \omega}{\partial x_j}, 10^{-20}\right]$$

In the previous equations, y is the distance to the next surface and D_ω^+ is the positive portion of the cross-diffusion term (to be introduced at a later stage).

Unlike the Standard k-ω model where the turbulent Prandtl numbers for k and ω (σ_k and σ_ω) are constants, in the SST k-ω model they are non-constants defined by:

$$\sigma_k = \frac{1}{\frac{F_1}{\sigma_{k,1}} + \frac{(1-F_1)}{\sigma_{k,2}}} \tag{22}$$

$$\sigma_\omega = \frac{1}{\frac{F_1}{\sigma_{\omega,1}} + \frac{(1-F_1)}{\sigma_{\omega,2}}} \tag{23}$$

F_2 is defined using the following:

$$F_2 = \tanh\left(\Phi_2^2\right)$$

$$\Phi_2 = \max\left[2\frac{\sqrt{k}}{0.09\omega y}, \frac{500\mu}{\rho y^2 \omega}\right]$$

Now returning to the cross-diffusion term, as the SST k-ω model is based upon both the Standard k-ω and the Standard k-ε model, the k-ε model has been transformed into equations based on k and ω, hence the cross-diffusion term, D_ω. This term is defined as:

$$D_\omega = 2(1-F_1)\rho\sigma_{\omega,2} \frac{1}{\omega} \frac{\partial k}{\partial x_j} \frac{\partial \omega}{\partial x_j} \tag{24}$$

Unlike the Standard k-ω model, however, the turbulent viscosity formulation is given for the high-Reynolds number form of the SST k-ω models as:

$$\mu_t = \frac{\rho k}{\omega} \frac{1}{\max\left[1, \frac{\Omega F_2}{a_1 \omega}\right]} \tag{25}$$

Where:

$$\Omega \equiv \sqrt{2\Omega_{ij}\Omega_{ij}}$$

The constants applied in the high Reynolds number form of the SST k-ω turbulence model are equal to:

$\sigma_{k,1} = 1.176$, $\sigma_{\omega,1} = 2.0$, $\sigma_{k,2} = 1.0$, $\sigma_{\omega,2} = 1.168$, $\alpha_1 = 0.31$, $\beta_{i,1} = 0.075$, $\beta_{i,2} = 0.0828$, $\kappa = 0.41$

4. Numerical Methods

4.1 Computational Domain and Mesh

The computational domain extended 1.5C upstream of the leading edge of the hydrofoil, 1.5C above and below the pressure surface and 3C downstream from the trailing edge. Velocity inlet boundary conditions were applied upstream, above and below the hydrofoil, while downstream an outflow boundary condition was used. The pressure and suction surfaces of the hydrofoil were defined independently with no-slip wall boundary conditions.

The selection of the boundary conditions and dimensions of the computational domain were an approximation to the free field. It was concluded that the flow boundary conditions were sufficiently distanced from the hydrofoil's surfaces such they should have little impact on the solution behaviour. The effect of the walls of the test section was considered by the method discussed in [1]. A free-stream velocity correction was calculated to be 1.045 for the 3m/s and 1.044 for 6 m/s

A finite volume method was employed to obtain a solution of the spatially averaged Navier-Stokes equations. The coupling between the pressure and velocity fields was achieved using the SIMPLE technique. A second-order upwind scheme was used for the convection and the central-differencing scheme for diffusion terms.

An unstructured mesh arrangement with quadrilateral elements was adopted to map the flow domain. Particular attention was directed to an offset 'inner region' encompassing the hydrofoil. Within this region a considerably fine O-type mesh was applied to achieve sufficient resolution of the hydrofoil surface and the boundary layer

region. Continuing downstream from the trailing edge of the inner region was the 'wake region'. A considerably fine H-type mesh was applied within this region to accurately resolve the near and far-wake flow behaviour. The remaining 'outer region' of the domain was discretized with a much coarser H-type mesh.

It should be noted that on the experimental hydrofoil used by Bourgoyne et. al. [1, 14 & 15], the trailing edge was ground to a 0.397mm radius, however, to allow improved surface discretization and mesh quality at the trailing edge of the numerical model this radius was increased to 1.5mm.

4.2 Model Parameters

The experimental hydrofoil was CNC machined from a solid casting of Ni-Al Bronze. The RMS surface roughness height, after polishing, was determined to be 2.5×10^{-7}m [14]. It was assumed that the roughness distribution was 'uniform sand-grain', allowing the use of a roughness constant of 0.5.

Information on the flow condition within the LCC's test section during the experimental testing was not explicitly detailed by Bourgoyne et. al. [1, 14 & 15], only that it was "a low turbulence water tunnel" [15]. From the literature [20] it was determined that the LCC's 'low turbulence' intensity was in the order of 0.1%. This value was assessed as reasonable and applied to all applicable boundary conditions.

4.3 Wall Treatments

4.3.1 Wall Functions

The application of wall functions to modelling the near-wall region may significantly reduce both the processing and storage requirements of a numerical model, while producing an acceptable degree of accuracy. The principal of the wall function is to 'bridge' the viscous flow near a wall and link the solution variables at the wall-adjacent cells to the corresponding quantities at the wall. With careful design of near wall mesh, wall functions should be applied where there are several cells within the boundary layer. Their use with excessively fine mesh near walls should be avoided as their validity expires within the viscous sublayer [13].

With respect to the non-dimensional wall parameter, y^+, a target value of 30 is desired of a mesh for the application of wall functions. This parameter is defined as:

$$y^+ = \frac{\rho\sqrt{\frac{\tau_w}{\rho_w}}y_p}{\mu} \tag{26}$$

In Equation (26), y_p is the distance from the first computational node to the wall and the subscript w denotes wall properties.

4.3.1.1 *Standard Wall Function*

The standard wall function applied is the logarithmic law-of-the-wall for mean velocity, given in the literature [13] as:

$$U^* = \frac{1}{\kappa}\ln\left(Ey^*\right) \tag{27}$$

Where:

$$y^* \equiv \frac{\rho C_\mu^{0.25} k_P^{0.5} y_P}{\mu}$$

k_P is the turbulence kinetic energy the cell centroidal node P and y_p is the distance from node P to the wall. κ and E are constants equal to 0.42 and 9.81 respectively.

For explicit detail on the computation of turbulence quantities in wall-adjacent cells using the standard wall function, the reader is directed to the literature [13]. Standard wall functions work reasonably well for a wide range of wall bounded flows, however, when the flow begins to diverge from ideal conditions, such as with strong adverse pressure gradients, the accuracy of their predictions is likely to degrade [13].

4.3.1.2 *Non-Equilibrium Wall Function*

The main differences between the standard wall function and the non-equilibrium wall function are that the law-of-the-wall for mean velocity is sensitised to pressure gradient effects and a two-layer-based concept is applied to calculate the cell-averaged turbulence kinetic energy production and dissipation in wall-adjacent cells [13].

The law-of-the-wall for mean velocity sensitised to pressure gradients is given in the literature [13] as:

$$\frac{\tilde{U}C_\mu^{0.25}k^{0.5}}{\tau_w/\rho} = \frac{1}{\kappa}\ln\left(E\frac{\rho C_\mu^{0.25}k^{0.5}y}{\mu}\right) \tag{28}$$

Where:

$$\tilde{U} = U - \frac{1}{2}\frac{\partial p}{\partial x}\left[\frac{y_v}{\rho\kappa\sqrt{k}}\ln\left(\frac{y}{y_v}\right) + \frac{y - y_v}{\rho\kappa\sqrt{k}} + \frac{y_v^2}{\mu}\right]$$

$$y_v \equiv \frac{\mu y_v^*}{\rho C_\mu^{0.25} k_P^{0.5}}$$

y_v^* is a constant equal to 11.225. For the cell-averaged turbulence kinetic energy production and dissipation in wall-adjacent cells, the two-layer concept assumes that the wall-adjacent cells consist of both a viscous sublayer and a fully turbulent layer [13]. Again for explicit detail on the computation of turbulence quantities in these cells using the non-equilibrium wall function, the reader is directed to the literature [13].

4.3.2 Enhanced Wall Treatment

Enhanced wall treatment is a method of near-wall modelling that utilises the combination of a two-layer zonal model with enhanced wall functions. This wall treatment is suitable for both considerably fine meshes and coarser meshes (or 'wall function meshes').

If the mesh is fine enough to resolve the laminar sublayer (within the order of $y^+ \approx 1$), then the wall treatment is identical to the two-layer zonal model, however, this mesh requirement can place significant demands on computational processing and storage infrastructure. For full details on the two-layer zonal model, the enhanced wall functions and their method of blending, the reader is directed to the literature [13]. Enhanced wall treatment with near-wall modelling is particularly required for flow scenarios involving severe pressure gradients leading to boundary layer separation [13].

5. Results and Discussion

5.1 Grid Independence Analysis

A grid independence analysis was conducted using four meshes of varying cell number. Each mesh was processed using the Realisable k-ε turbulence model with enhanced wall treatment, at a free-stream velocity of 3m/s (Re = 8.284×10^6). Table 1 details the node and y^+ characteristics of each mesh, highlighting the refinements between the subsequent meshes *A*, *B*, *C* and *D*.

Both mesh *C* and mesh *D* achieve considerably low average y^+ values, sufficiently resolving the laminar sublayer (i.e. $y^+ \leq 4$–5). Although having a minimum y^+ value well within the laminar sublayer, the maximum and average values of mesh *B* indicate

that its resolution extends to the buffer layer only (i.e. $5 \leq y^+ \leq 30$). Also with a sufficiently low minimum y^+, mesh *A* shows significant coarseness with considerably larger maximum and average y^+ values, indicating resolution to the turbulent outer layer only (i.e. $y^+ \geq 30$).

Table 2 shows the predicted pressure-derived lift and drag coefficients, and the respective percentage error from the experimental values for each mesh. The application of each mesh generally produces accurate predictions of the lift and drag coefficients with comparison to the experimental data. It can be seen that the error associated with the predicted lift coefficient decreases with mesh refinement, however, at the same time an increase in error of the predicted drag coefficient is shown. With the use of mesh *C* and mesh *D* predicting almost identical coefficients, this suggests that the solution has converged and grid independence has been achieved.

Figure 3 displays the pressure surface boundary layer normalised mean velocity profiles at 93%C, predicted using each mesh. With comparison to the experimental data, the velocity profile was slightly under-predicted, but generally well resolved using each mesh. The velocity profiles predicted using mesh *C* and mesh *D* are identical and show clear differences from those of mesh *A* and mesh *B*, again suggesting grid independence with the two finest meshes.

Therefore, with mesh *C* and mesh *D* predicting almost identical results, it is concluded that a suitable degree of grid independence is shown by the numerical solution. In consideration of the processing infrastructure and time constraints, the very marginal performance advantages provided by the finest mesh (mesh *D*) do not justify the increased cell numbers ($\approx$ 16%) and extended CPU processing times. Henceforth, all numerical solutions discussed are obtained using mesh *C*.

5.2 Turbulence Model Performance

The results of the performance of each turbulence model are presented with respect to the predicted pressure coefficient distribution, lift and drag coefficients, the pressure surface boundary layer, suction surface boundary layer separation and the trailing edge and far-wake flow. The performance of each turbulence model is assessed at chord-based Reynolds numbers of 8.284×10^6 (U_∞= 3m/s) and 1.657×10^7 (U_∞= 6m/s).

NOTE: All presented data is dimensionless: co-ordinate locations are referenced to the chord length (i.e. *x*/C and *y*/C) and all mean velocities are normalised with the free-stream velocity.

5.2.1 Coefficients of Pressure, Lift and Drag

Figure 4 illustrates the pressure coefficient distribution at the surface of the hydrofoil as predicted by each turbulence model, at a free-stream velocity of 3m/s (A negative

scale is used to enable easier comparison with the physical surfaces of the hydrofoil). The distributions predicted by the Realisable k-ε and the SST k-ω models are very encouraging, however, the Standard k-ε and Standard k-ω models show significant deviation from the experimental data.

The Realisable k-ε turbulence model predicts high-pressure (referenced to the free-stream static pressure) below the hydrofoil and low-pressure above, whereas the SST k-ω model predicts low-pressure both above and below. This indicates that the Realisable k-ε model predicts decreased flow velocity below the pressure surface and increased flow velocity above the suction surface, whereas the SST k-ω predicts increased flow velocity both above and below the hydrofoil.

Both of these flow scenarios are valid, being dependent on the camber and thickness characteristics, however, as these variables are fixed, all turbulence models should predict the same flow behaviour. Comparison to the experimental data demonstrates that the Realisable k-ε model excellently predicts the flow behaviour below the pressure surface. This model also performs exceptionally well at the leading edge, accurately predicting the stagnation conditions. However poorer correlation is shown at the trailing edge. Over the larger suction surface the Realisable k-ε model under predicts the magnitude of the low static pressure region. The net effect of this is to reduce the pressure-induced force acting on the suction surface, hence the net lift force and the lift coefficient.

The SST k-ω turbulence model shows very similar qualitative characteristics as to those predicted by the Realisable k-ε model. However, the predicted pressure coefficient distribution is translated upwards. This translation results in the SST k-ω model more closely predicting the pressure coefficient distribution on the suction surface. However, a poorer correlation is shown with the experimental data in the leading and trailing edge regions, and at the pressure surface.

Similarly, the Standard k-ε and Standard k-ω models predict almost identical qualitative characteristics of the pressure coefficient distribution as to those predicted by the previously discussed models. However, both models significantly over-predict the pressure coefficient distribution, indicating vastly different behaviour of the flow around the hydrofoil with respect to the experimental data.

These two models predict considerably low-pressure regions both above and below the hydrofoil. The results are significantly lower in magnitude than those predicted by either the Realisable k-ε or SST k-ω turbulence models. This suggests that both models predict significant flow accelerations both above and below the hydrofoil. It is expected that this is caused by the excessive level of turbulent viscosity, which has also been observed by other researchers [4,7].

With such deviations from the experimental data, the pressure coefficient distributions predicted by the Standard k-ε and Standard k-ω turbulence models are viewed with considerable concern.

Inspection of the predicted pressure coefficient distribution at a free-stream velocity of 6m/s (illustrated in Figure 5) reveals identical predictions by each turbulence model as at 3m/s. Again the Realisable k-ε turbulence model most accurately predicts the experimental data, while the Standard k-ε and Standard k-ω models show considerable error in their predictions.

It is concluded that the errors associated with the pressure coefficient distributions predicted by the Standard k-ε and Standard k-ω turbulence models are not associated with post-processing error for two reasons. Firstly, the stagnation conditions are correctly predicted (i.e. $-C_P \approx -1$) by each model and secondly, variations of similar magnitudes are present in the reported pressure forces acting on the individual surfaces of the hydrofoil, detailed in Table 3 and Table 4, for free-stream velocities of 3m/s and 6m/s respectively.

Although the net lift forces predicted by each turbulence model are very similar, the forces on the individual surfaces vary significantly. The Realisable k-ε model predicts 12.36kN and 49.47kN acting on the suction surface at free-stream velocities of 3m/s and 6m/s respectively, however, the Standard k-ω model predicts respective values of 51.13kN and 186.74kN, values approximately four times greater. Again this characteristic is in accordance with other researchers [4,7] observations the Standard k-ε and Standard k-ω turbulence models over-predict the level of turbulent viscosity.

Therefore, it is assumed that this is an accurate representation of the performance of each turbulence model in predicting the pressure coefficient distribution of the hydrofoil.

Table 5 displays the pressure-derived lift and drag coefficients predicted by each turbulence model at a free-stream velocity of 3m/s. Percentage error from the experimental values are indicated. Each turbulence model generally acceptably predicts the lift coefficient, although the accuracy trend of each model shown in the pressure coefficient distribution was not replicated as expected. The most accurate turbulence model was the Standard k-ε, which predicted the hydrofoils lift coefficient to within 1.34% of the experimental value. As expected from the analysis of the pressure coefficient distribution (Figure 4), the Realisable k-ε model under-predicts the lift coefficient by 4.11%.

With consideration to the pressure coefficient distribution, a better indication of each turbulence model's performance is gained from the predicted drag coefficients. It is evident that the errors associated with the Standard k-ε and Standard k-ω turbulence models in predicting the pressure coefficient distribution (although not greatly affecting the predicted coefficients of lift) have considerable impact on the predicted

drag coefficients. The accuracy trend of the turbulence models is identical to that shown by the pressure coefficient distribution; the Realisable k-ε model predicts the drag coefficient most accurately (to within 11.11% of the experimental value) and the Standard k-ω model the least accurately (444.44%).

Table 6 displays the pressure-derived lift and drag coefficients predicted by each turbulence model at a free-stream velocity of 6m/s. At this flow velocity, each turbulence model reasonably predicts the lift coefficient and again a misleading performance trend is shown.

Comparison to the numerical data at a free-stream velocity of 3m/s (Table 5) shows that an increase in Reynolds number results in improvements in the performance of each turbulence model. The magnitude of error associated with the lift coefficient predicted by the Standard k-ε, the Realisable k-ε, the Standard k-ω and the SST k-ω models decreased by 0.31%, 2.63%, 2.8% and 2.28% respectively. For the predicted drag coefficient, however, the error associated with both the Standard k-ε and SST k-ω models increased by 13.02% and 5.69% respectively, whereas that of the Realisable k-ε and Standard k-ω models showed slightly improved predictions by 0.26% (11.11% to 10.85%) and 40.58% (444.44% to 403.87%) respectively.

In summary, the presented data of the predicted pressure coefficient distribution and the lift and drag coefficients at free-stream velocities of 3m/s ($Re = 8.284\times10^6$) and 6m/s ($Re = 1.657\times10^7$), the Realisable k-ε turbulence model clearly outperforms the remaining turbulence models. This model also consistently shows equal, if not slightly improved, predictions at the higher Reynolds number.

5.2.2 Pressure Surface Boundary Layer

Figure 6 illustrates the numerical and experimental pressure surface boundary layer velocity profiles at 93%C at a free-stream velocity of 3m/s. The results have been inverted to enable comparison. As the pressure surface is largely flat beyond 28%C with only moderate surface gradients prior to this point, it can be approximated as a flat plate. Therefore, also shown in Figure 6 is the theoretically predicted turbulent boundary layer velocity profile, calculated using classical turbulent boundary layer equations [21].

Each turbulence model predicts a differing velocity profile with varying degrees of correlation to the experimental data. Good correlation is shown by the theoretical velocity profile with accurate predictions of both the velocity gradient and the boundary layer thickness (defined as the endpoint of the profile).

The Standard k-ε, Standard k-ω and SST k-ω turbulence models all produce smoothly changing profiles that slightly over-predict the velocities closer to the surface (i.e. $y/C < 0.009$) and under-predict further away from the surface.

The turbulence model that most accurately predicts the boundary layer velocity profile is the Realisable k-ε model. Close to the surface (i.e. $y/C < 0.005$) this model predicts the boundary layer characteristics exceptionally well and continues to maintain a high degree of correlation further from the surface. Unlike the other turbulence models, the Realisable k-ε model produces a definable gradient change where the velocity profile becomes quite blunt. The approximate location where the velocity profile exhibits this characteristic visually correlates well to the experimental and theoretical boundary layer thicknesses (i.e. $u \approx 99\%U_\infty$).

Table 7 details the boundary layer parameters derived from the numerical data of each turbulence model, and presents a comparison with the experimental and theoretical parameters at a free-stream velocity of 3m/s.

The superior performance of the Realisable k-ε model is highlighted in Table 7. The boundary layer thickness and displacement thickness are predicted within 6.18% and 9.60% respectively. The SST k-ω model predicts these parameters to within 27.68% and 16.16% respectively, whilst the Standard k-ε and Standard k-ω turbulence models significantly over-predicted the boundary layer thickness (164.25% and 291.02% respectively) and over-predict the displacement thickness (16.86% and 15.69% respectively).

Figure 7 illustrates the same pressure surface boundary layer profiles at 93%C, at a free-stream velocity of 6m/s. Again the Realisable k-ε turbulence model excellently predicts the boundary layer velocity profile. Slight over-predictions are noted closer to the surface (i.e. $y/C < 0.009$). A poorer correlation to the experimental data is shown by the theoretically calculated velocity profile, as the Reynolds number of the flow is slightly greater than the valid Reynolds number range of the equation [21]. The Standard k-ε, Standard k-ω and SST k-ω turbulence models again all produce smoothly changing velocity profiles that over-predict the experimental velocity profile closer to the surface.

Similarly to Table 7, Table 8 details the boundary layer parameters at a free-stream velocity of 6m/s. Given that the uncertainty of the experimental data, measured a boundary thickness for 6m/s greater than that for 3m/s, the comparison with experimental data seems unnecessary. However, in Table 8, the experimental data was listed as a reference. All models correctly predict decreasing boundary layer thickness with increasing Reynolds number, except the SST k-ω turbulence model, which predicts a greater boundary layer thickness at 6m/s (38.06mm) compared to that at 3m/s (37.82mm).

Both the Standard k-ε and Standard k-ω turbulence models again performed considerably poorly, significantly over-predicting both the boundary layer thicknesses and the displacement thicknesses. Like the SST k-ω model these models incorrectly predict the trend of the boundary layer thickness with increasing Reynolds number.

In summary of the predictions of the pressure surface boundary layer at 93%C at free-stream velocities of both 3m/s and 6m/s, the Realizable k-ε turbulence model clearly outperforms the Standard k-ε, Standard k-ω and SST k-ω models. This model predicts the velocity profile, boundary layer thickness and displacement thickness to a high degree, and was the sole turbulence model to predict boundary layer thinning with increasing Reynolds number.

5.2.3 Suction Surface Boundary Layer Separation

To assess if each turbulence model correctly predicts suction surface boundary layer separation, analysis of the coefficient of skin friction on the surfaces of the hydrofoil was completed. For a two-dimensional steady-state flow, the full separation point (S) of the boundary layer can be approximately defined where the wall shear stress, hence the skin-friction coefficient, becomes zero [21].

Figure 8 illustrates the skin-friction coefficient distribution on the suction surface at the trailing edge for a free-stream velocity of 3m/s. Experimentally, boundary layer separation was determined to occur between 95.75%C and 97.50%C on the suction surface of the hydrofoil [1].

Both the Realisable k-ε and SST k-ω turbulence models, and the Standard k-ε and Standard k-ω turbulence models predict different skin-friction coefficient magnitudes in the vicinity of the trailing edge. However, distinctive features predicted by each turbulence model occur at very similar chord-wise locations.

At approximately 96.5%C, all models predict a fluctuating increase in the skin-friction coefficient, peaking at a chord-wise location of 96.82%C. It is considered that these fluctuations are associated with the combined effects of the considerably fine mesh and the surface discontinuities introduced when the trailing edge was modified. Directly following the skin-friction coefficient peak is a steep decrease, reaching zero at a chord-wise location of between 97.86%C and 98.52%C (depending on the turbulence model). Beyond this chord-wise location, a small secondary increase of the skin-friction coefficient occurs, followed by a gradual decrease to zero at the trailing edge (In Figure 8, the trailing edge terminates just prior to 100%C due to the fillet radius).

It is considered that the fluctuating increase then sharp decrease in the skin friction coefficient is associated with the commencement of suction surface boundary layer separation at the commencement of the trailing edge modifications at 96.75%C. The steep adverse pressure gradient within this region begins to significantly retard the motion of fluid particles adjacent to the surface reducing their velocity, hence the wall shear stress and the coefficient of skin friction.

The first chord-wise location where the skin friction coefficient steeply decreases to zero is considered to be the location at which the boundary layer flow adjacent to the surface stagnates. This indicates that the fluid particles within the boundary layer flow directly adjacent to the surface are halted through the combined effects of the adverse pressure gradient and backflow from the recirculation bubble. The second chord-wise location where the skin-friction coefficient tends to zero again indicates flow stagnation and the partial reattachment of the boundary layer flow. The chord-wise distance between these two points of boundary layer flow stagnation defines the length of the recirculation bubble.

As all turbulence models predict the commencement of suction surface boundary layer separation at the start of the modified trailing edge (i.e. ≈96.75%C), the only variation between each models performance is the prediction of the chord-wise location of full boundary layer separation (i.e. the first location of zero skin-friction and boundary layer flow stagnation), hence the chord-wise size of the recirculation bubble.

The Standard k-ε, Realisable k-ε, Standard k-ω and SST k-ω turbulence models predict full boundary layer separation at chord-wise locations of 98.59%C, 98.37%C, 98.31%C and 98.15%C respectively. Therefore, the Standard k-ε model predicts the smallest recirculation bubble, whereas the SST k-ω predicts the largest. Although these locations are slightly over-predicted with comparison to the separation location range predicted experimentally (i.e. 95.75%C < S > 97.50%C), the point at which boundary layer separation commences correlates well.

Figure 9 illustrates the skin-friction coefficient distribution on the suction surface at the trailing edge for a free-stream velocity of 6m/s. Similar to the coefficient of skin friction characteristics at 3m/s, the Realisable k-ε and SST k-ω turbulence models, and the Standard k-ε and Standard k-ω turbulence models again predict different magnitudes in the vicinity of the trailing edge. Again the rapid decrease in the skin-friction coefficient, indicating the commencement of boundary layer separation, is predicted at approximately 96.55%C by each turbulence model. This suggests that the separation commencement location is independent of Reynolds number and that the trailing edge geometry is the dominant variable in its location.

Similarly, two locations where the skin friction coefficient equalled zero were predicted on the trailing edge curve. The predicted locations of full boundary layer separation by the Standard k-ε, Realisable k-ε, Standard k-ω and SST k-ω turbulence models, are 98.75%C, 98.48%C, 98.48%C and 98.31%C respectively. When compared with the respective chord-wise locations at 3m/s, each location of full boundary layer separation shifts closer to the trailing edge by 0.16%C, 0.11%C, 0.17%C and 0.16%C respectively. Again the Standard k-ε predicted the smallest recirculation bubble and the SST k-ω model predicted the largest.

This suggests that with increasing Reynolds number and a fixed commencement point of boundary layer separation, the location at which the boundary layer flow fully

separates moves rearwards, confirming the experimental observations of both Bourgoyne et. al. [1] and Baubeau & Latorre [17].

In summary, each turbulence model accurately predicts the commencement location of boundary layer separation and that the location of full separation moves rearwards with increasing Reynolds number. Although it is not possible to determine the turbulence model that provides superior performance with respect to the experimental data, the solution convergence shown by both the Realisable k-ε and SST k-ω models at both 3m/s and 6m/s indicates a more confident prediction of the skin friction coefficient in the trailing edge region.

5.2.4 Trailing Edge and Wake Flow

To assess the performance of each turbulence model in predicting the flow characteristics in the near and far wake, the normalised stream-wise mean velocity profiles at three chord-wise planes in the near wake and one in the far wake are discussed for free-stream velocities of 3m/s and 6m/s.

Figure 10 illustrates the normalised stream-wise mean velocity profile within the trailing edge region at chord-wise location of 97.8%C. This plane is located between the start of the trailing edge modifications (96.75%C) and the tip of the trailing edge, prior to the point of full boundary layer separation.

The Standard k-ω, Standard k-ε, and the SST k-ω models generally perform poorly within this region, under-predicting the velocities above and below the trailing edge surfaces, possibly suggesting that the models are too diffusive. The Realisable k-ε model, however, shows encouraging performance in resolving the important flow features. This model predicts the steep velocity gradient changes through the separating boundary layer flow. Below the pressure surface, improved performance is shown by the Realisable k-ε model in predicting the pressure surface boundary layer flow near the trailing edge tip. This model is the only model to accurately predict a slight 'surge' in the velocity profile, located near $y/C \approx 0.018$.

Figure 11 illustrates the normalised stream-wise mean velocity profile within the trailing edge region at the tip of the hydrofoil (i.e. 100%C), a region of considerable turbulent flow activity. Although accurately predicting the magnitude of the flow reversal associated with the recirculation bubble, the Standard k-ε, Standard k-ω and SST k-ω turbulence models show poor correlation to the experimental data. Again neither of these models predict the steep velocity gradient changes through the recirculation bubble and below the pressure surface. The Standard k-ε and Standard k-ω models show considerable error above the suction surface.

The Realisable k-ε model accurately predicts the magnitude of the flow reversal and shows excellent correlation to the experimental data below the trailing edge, again

accurately predicting the velocity profile 'surge'. Above the trailing edge, the correlation to the experimental data degrades marginally with an over prediction in the transverse thickness of the recirculation bubble.

Figure 12 illustrates the normalised stream-wise mean velocity profile just downstream of the hydrofoil's trailing edge at 102.8%C, within the near wake region. In general, a poorer velocity profile prediction is shown by each turbulence model compared with previous chord-wise locations. All models over-predict the minimum velocity at the core of the wake and under-predict the transverse thickness of the wake region, showing poor correlation to the experimental data above the trailing edge. The Realisable k-ε turbulence model is the only model to successfully predict the steep velocity gradient changes through the wake core. However, beyond the wake core it slightly over predicts the velocity profile.

Figure 13 illustrates the normalised stream-wise mean velocity at 150%C within the far wake, a region of continuing turbulent kinetic energy dissipation. When compared with the turbulence model performance observed in the near wake (Figure 12) and the over-prediction of the minimum velocity, all models in the far wake under-predict the minimum velocity within the wake core. Again the velocity profile predicted by the Standard k-ε and Standard k-ω models are considerably poor. The Realisable k-ε model predicts almost instantaneous velocity gradient changes through the wake core, while the SST k-ω model predicts steep, yet more gradual velocity gradient changes, suggesting that both models posses very low damping. Both models generally show good correlation to the experimental data, particularly within the wake core. The 'downwash' effect of the flow over the hydrofoil is generally well predicted by each turbulence model, with the wake core being translated downwards with respect to its previous position in the near wake (Figure 12).

For analysis of the trailing edge and wake flow at a higher Reynolds number, Figure 14, Figure 15, Figure 16 and Figure 17 illustrate the normalised stream-wise mean velocity profiles at 97.8%C, 100%C, 102.8%C and 150%C respectively, at a free-stream velocity of 6m/s, correlating to Re = 1.657×10^7.

When compared with the performance predicted at the low velocity (Figure 10), a distinct improvement is achieved by the Realisable k-ε turbulence model (Figure 14). It can be seen in Figure 14 that above the suction surface the Realisable k-ε model shows considerable improvement in predicting the separating boundary layer flow, while below the pressure surface the pressure surface boundary layer is more accurately resolved. The results presented in Figure 10 indicates that the remaining turbulence models have considerable difficulty in predicting the steep velocity gradient changes through the boundary layer flow both above and below the trailing edge surfaces.

Similar performance improvements are shown by the Realisable k-ε model in Figure 15, at a chord-wise location of 100%C. The accuracy of the predicted flow reversal in the recirculation bubble is lower than at 3m/s, however a higher degree of correlation to

the experimental velocity profile is shown through the recirculation bubble and the pressure surface boundary layer. Although the SST k-ω model more accurately predicts the degree of flow reversal, it again has difficulty resolving the steep velocity gradient changes through both the recirculation bubble and the pressure surface boundary layer.

Within the near wake at a chord-wise location of 102.8%C (Figure 16), again a generally a poorer velocity profile prediction is shown by each turbulence model compared to the previous chord-wise planes (Figure 14 and Figure 15). All models again over-predict the minimum velocity at the core of the wake and under-predict the transverse thickness of the wake region, with the poorest correlation to the experimental data occurring above the trailing edge. A considerable improvement is shown by the Realisable k-ε model in predicting the velocity gradient changes through the wake core and the velocities beyond the wake core.

Figure 17 illustrates the normalised stream-wise mean velocity profile in the far wake region at 150%C. Again as present within the near and far wake velocity profiles at 3m/s (Figures 10, 11, 12, and 13), it appears that the performance of each turbulence model degrades within the wake region with increasing distance downstream from the hydrofoil. Again the Standard k-ε, Standard k-ω and the SST k-ω models show poor correlation to the experimental velocity profile. The Realisable k-ε model acceptably predicts the experimental velocity profile within the wake core, with consideration to the applied scale. Beyond the wake core, marginal over-predictions in the velocity profile are shown.

In summary, when comparing the performance of each turbulence model in predicting the flow characteristics in the near and far wake, it is apparent that the Realisable k-ε turbulence model predicts superior velocity profiles. The distinct advantage of this model compared with the Standard k-ε, Standard k-ω and SST k-ω models, is that the steep velocity gradient changes through the separating boundary layer flow, the recirculation bubble, and in the near and far wakes, are accurately resolved. Although the Realisable k-ε model produces accurate predictions at 3m/s ($Re = 8.284\times10^6$), it shows considerably improved performance at 6m/s ($Re = 1.657\times10^7$).

5.3 Analysis of Wall Treatments

The results of the performance of the Realisable k-ε turbulence model using the three wall treatments (the standard and non-equilibrium variants, and the enhanced wall treatment employing near-wall modelling techniques), are presented at a free-stream velocity of 3m/s ($Re = 8.284\times10^6$). The results presented include the predicted pressure coefficient distribution, the lift and drag coefficients, and the pressure surface boundary layer.

Figure 18 illustrates the coefficient of pressure distribution at the surface of the hydrofoil, predicted using the three different wall treatments. It is clear that the use of the wall treatments impacts upon the solution behaviour. As expected in flow scenarios involving strong adverse pressure gradients and boundary layer separation, the enhanced wall treatment produces the most accurate distribution. The use of the standard wall function produces a slightly less accurate prediction, yet performs generally well at the leading and trailing edges. However, the use of the non-equilibrium wall functions produces questionable results, particularly at the leading edge where the coefficient of pressure distributions on the suction and pressure surfaces cross each other.

Similarly to the coefficient of pressure distribution, the wall treatment has a marked effect on the predicted lift and drag coefficients. Table 9 displays the pressure-derived coefficients of lift and drag predicted by each wall treatment at a free-stream velocity of 3m/s.

Using the standard wall function, the coefficient of lift is largely under-predicted by 17.95%. However, this wall treatment produces a surprisingly accurate prediction of the coefficient of drag, only under-predicting the experimental value by 3.70%. Much poorer predictions are shown using the non-equilibrium wall functions, under-predicting the coefficient of lift by 28.75% and over predicting the coefficient of drag by 33.33%. The use of enhanced wall treatments produces generally accurate predictions of both the lift and drag coefficients to within 4.11% and 11.11% respectively.

Figure 19 illustrates the numerical, experimental and theoretical pressure surface boundary layer velocity profiles at 93%C, at a free-stream velocity of 3m/s. As expected in the near wall region, the use of each wall treatment predicts a different boundary layer velocity profile.

Again the use of enhanced wall treatment produces the most accurate velocity profile when compared with the experimental data. The use of the standard wall function produces a boundary layer velocity profile with similar features to those produced by the enhanced wall treatment, however a larger boundary layer thickness is predicted. Again, similar features are predicted using the non-equilibrium wall function and, again a much greater boundary layer thickness is predicted. The use of the enhanced wall treatment predicts the boundary layer thickness to within 6.18%, whereas the standard wall function and non-equilibrium wall function produce predictions to within 15.26% and 37.54% respectively.

These results obtained using the three different wall treatments reaffirm the guidelines for the application of wall treatments to certain meshes and flow scenarios. With an average y^+ value of 2.31, the mesh used for this analysis is particularly fine (less than the desired value of 30) and is not classed as a 'wall function mesh'. Therefore, the validity of wall functions applied to this mesh is significantly degraded, producing poor numerical results. It is apparent that the standard wall function copes best in such

an adverse application, whereas the non-equilibrium wall function performs rather poorly.

6. Concluding Remarks

Evaluation of the Standard k-ε, Realisable k-ε, Standard k-ω and the SST k-ω RANS turbulence models against high quality experimental data, has revealed that the Realisable k-ε model shows vastly superior performance when applied in the steady-state analysis of hydrofoil turbulent boundary layer separation at high Reynolds numbers of 8.284×10^6 (3m/s) and 1.657×10^6 (6m/s).

The Realisable k-ε turbulence model accurately predicts the pressure coefficient distribution at the surface of the hydrofoil, leading to good predictions in the overall pressure-derived lift and drag coefficients. Analysis of the turbulent boundary layer on the pressure surface of the hydrofoil at 93%C shows that the Realisable k-ε model resolves the velocity profile, the boundary layer thickness and displacement thickness to a high degree. This model is also the only model to correctly predict boundary layer thinning with an increase in Reynolds number.

Suction surface boundary layer separation from the trailing edge is also well predicted by the Realisable k-ε turbulence model. The commencement location of boundary layer separation is accurately predicted, and this model correctly predicts that the full separation point of the turbulent boundary layer moves rearward with increasing Reynolds number.

Even in the challenging separated trailing edge and near wake regions, the Realisable k-ε model accurately predicts the normalised stream-wise mean velocity profiles at four chord-wise planar locations. The distinct performance advantage offered by the Realisable k-ε model at these locations that it accurately predicts the steep velocity gradient changes through the separating boundary layer flow, the recirculation bubble and the wake core in the near region.

The comparison of the respective results at Reynolds numbers of 8.284×10^6 (3m/s) and 1.657×10^6 (6m/s) indicates that the performance of the Realisable k-ε model shows improvement with an increase in Reynolds number. Predictions of the hydrofoils overall coefficients of lift and drag show improvement, the pressure surface boundary layer parameters are more accurately predicted, and considerable improvement is shown in the prediction of the normalised stream-wise mean velocity profiles in the near and far wakes.

Furthermore analysis of three different wall treatments (standard and non-equilibrium wall functions, and enhanced wall treatment with near-wall modelling), indicates that for flows involving severe adverse pressure gradients and boundary layer separation,

the application of enhanced wall treatment may be preferable for producing accurate results. Confirming the guidance provided in the literature [13], the application of wall functions to a considerably fine mesh significantly degrades their validity, producing poor numerical results.

Therefore, the application of the Realisable k-ε turbulence model with enhanced wall treatment to high-Reynolds number hydrodynamic flow scenarios, involving adverse pressure gradients and boundary layer separation, may provide researchers with more encouraging results from numerical methods.

Acknowledgements

This work was supported through a collaborative research agreement between the Maritime Platforms Division (MPD) of the Defence Science and Technology Organisation (DSTO) and the School of Aerospace, Mechanical and Manufacturing Engineering at RMIT University.

7. References

1. Bourgoyne, D.A., Ceccio, S.L., Dowling, D.R., Jessup, S., Park, J., Brewer, W., and Pankajakshan, R. 2000, "*Hydrofoil turbulent boundary layer separation at high Reynolds numbers*", 23rd Symposium on Naval Hydrodynamics, Val de Reuil, France.

2. Newman, J.N. 1978, "*Marine Hydrodynamics*", Massachusetts Institute of Technology, Massachusetts, USA, p. 95.

3. Arabshahi, A., Beddhu, M., Briley, W., Chen, J., Gaither, A., Janus, J., Jiang, M., Marcum, D., McGinley, J., Pankajakshan, R., Remotigue, M., Sheng, C., Sreenivas, K., Taylor, L., Whitfield, D. 2000, "*A Perspective on Naval Hydrodynamic Flow Simulations*", 22nd Symposium on Naval Hydrodynamics, Washington D.C., USA, pp. 920-932.

4. Speziale, C.G., Abid, R. & Anderson, E.C. 1992, "*Critical Evaluation of Two-Equation Models for Near-Wall Turbulence*", AIAA J., Vol. 30 No. 2, pp. 324-331.

5. Wilcox, D.C. 1988, "*Reassessment of the scale-determining equation for advanced turbulence models*", AIAA J., Vol. 26 No. 11, pp. 1299-1310.

6. Wilcox, D.C. 1988, "*Multi-scale model of turbulent flows*", AIAA J., Vol. 26, pp. 1311-1320.

7. Lien, F.S. & Leshziner, M.A. 1995, "*Modelling 2D separation from a high-lift aerofoil with a non-linear eddy-viscosity model and second-moment closure*", Aeronautical Journal, April, pp. 125-143.

8. Shih, T.H., Zhu, J. & Lumley, J.L. 1993, "*A realisable Reynolds stress algebraic equation model*", NASA TM-105993.

9. Pajayakrit, P. & Kind, R.J. 2000, "*Assessment and Modification of Two-Equation Turbulence Models*", AIAA J., Vol. 38 No. 6, pp. 955-963.

10. Baldwin, B. & Lomax, H. 1978, "*Thin-layer approximation and algebraic model for separated turbulent flows*", AIAA Paper 78-257.

11. Dash, S.M., Beddini, R.A., Wolf, D.E. and Sinha, N. 1983, "*Viscous/inviscid analysis of curved sub or super-sonic wall jets*", AIAA Paper 83-1697.

12. Kim, W.J., Kim, D.H. & Van, S.H. 2002, "*Computational study on turbulent flows around modern tanker hull forms*", International Journal for Numerical Methods in Fluids, Vol. 38, pp. 377-406.

13. Fluent Inc. 2001, "*FLUENT 6.0 User's Guide*", NH, USA.

14. Bourgoyne, D.A., Ceccio, S.L., Dowling, D.R., Hamel, J.M., and Judge, C.Q. 2001a, "*Lifting surface flow, pressure and vibration at high Reynolds-number*", ASME International Conference and Exposition, New York, USA.

15. Bourgoyne, D.A., Ceccio, S.L., Dowling, D.R., Hamel, J.M., and Judge, C.Q. 2001b, "*Hydrofoil testing at high Reynolds number*", CP, Department of Mechanical Engineering, University of Michigan, Michigan, USA.

16. Gorski, J. & Nguyen, P. 1991, "*Navier-Stokes Analysis of Turbulent Boundary Layer Wake for Two-Dimensional Lifting Bodies*", Eighteenth Symposium on Naval Hydrodynamics, Ann Abor, USA, pp. 633-643.

17. Baubeau, R. & Latorre, R. 1986, "*Numerical Study of the Boundary Layer Transition for Two-Dimensional NACA 16-012 and 4412 Hydrofoil Sections*", Journal of Ship Research, Vol. 30 No. 1, pp. 43-50.

18. Baubeau, R. & Latorre, R. 1990, "*Numerical Study of Wall Influence on Boundary Layer Transition for Two-Dimensional NACA 16-012 and 4412 Hydrofoil Sections*", Journal of Ship Research, Vol. 34 No. 1, pp. 38-47.

19. Baubeau, R. & Latorre, R. 1995, "*Numerical study of Hydrofoil Boundary Layers*", Ocean Engineering, Vol. 22 No. 1, pp. 87-95.

20. Internet Reference

www.dt.navy.mil/div/capabilities/facilities/5004.html

(Accessed: 4th of August, 2002)

21. Gersten, K. & Schlichting, H. 2000, "*Boundary Layer Theory*", 8th Ed., Springer-Verlag, Berlin, Germany.

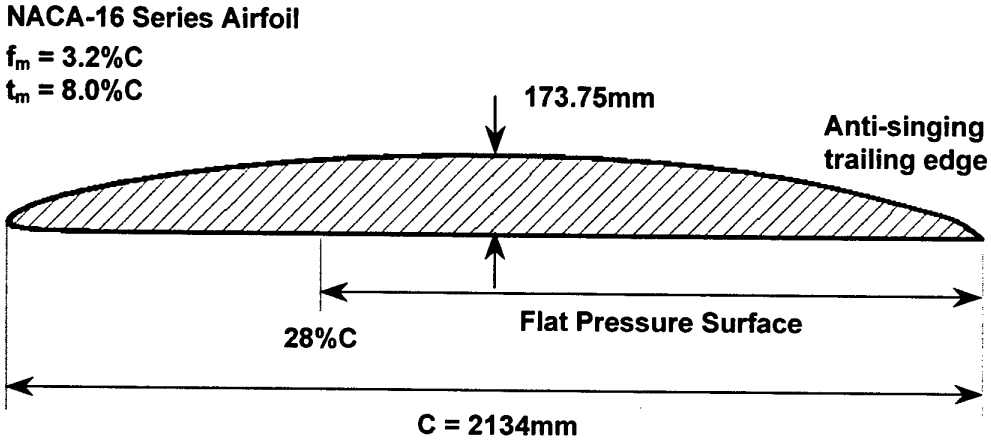

Figure 1. The two-dimensional hydrofoil geometry as used by Bourgoyne et. al. [1, 14 and 15] (Adapted from 1)

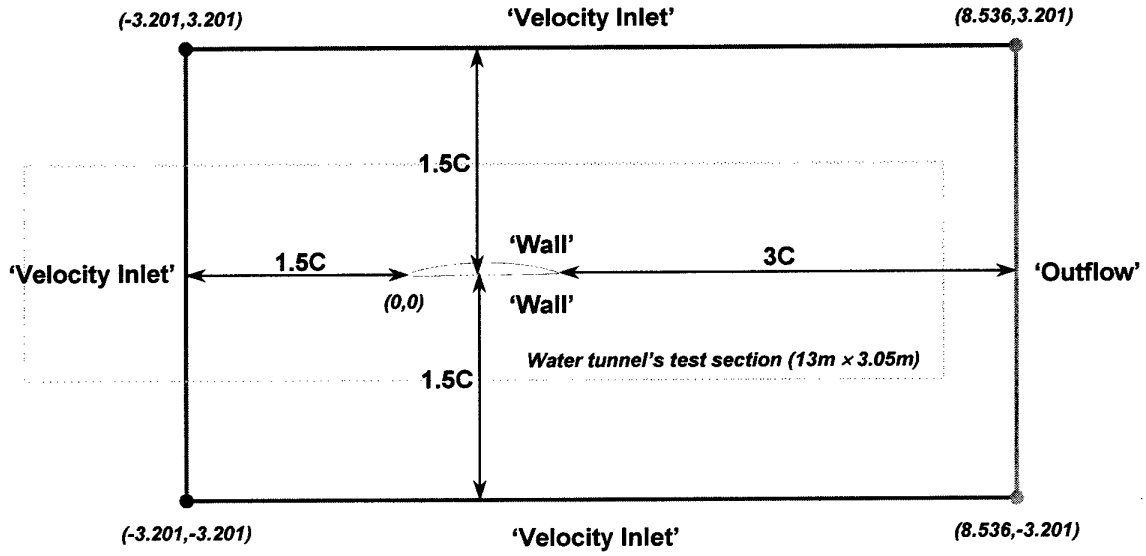

Figure 2. The dimensions and boundary conditions of the computational domain, including the dimensions of the water tunnel's test section (in which the hydrofoil was centrally positioned)

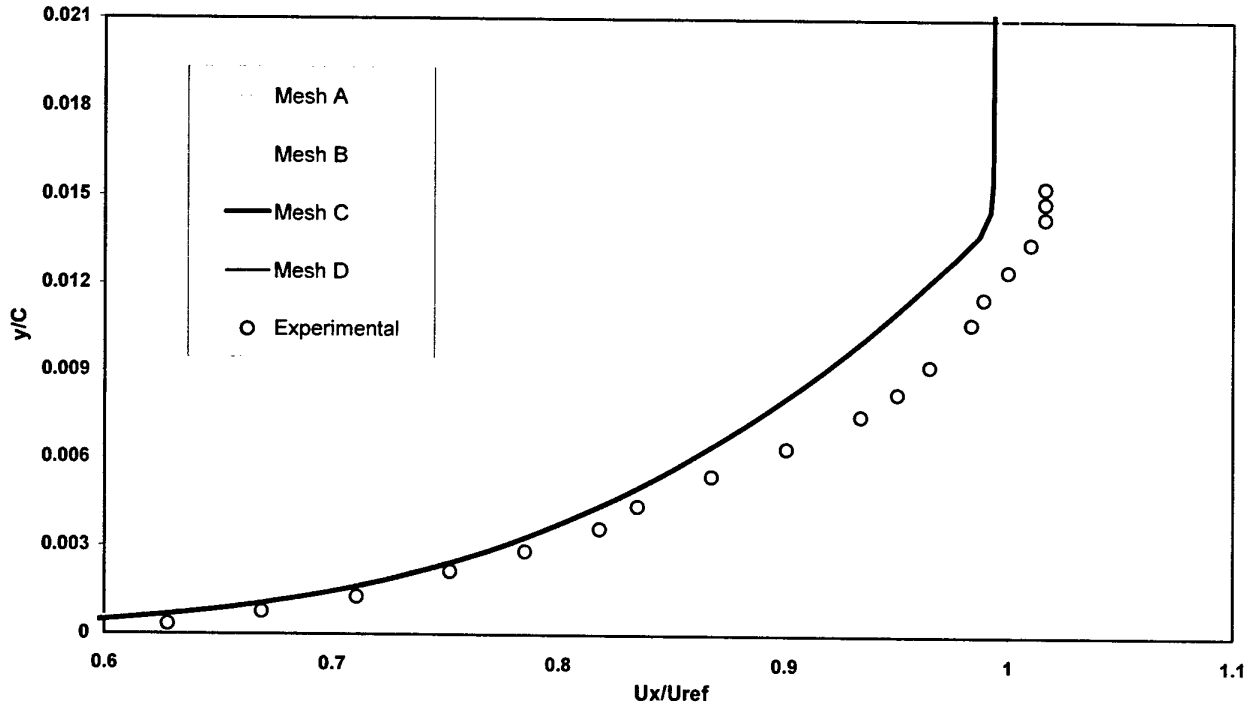

Figure 3. Grid Independence Analysis: Pressure surface boundary layer normalised stream-wise mean velocity profile at 93%C (U_∞= 3m/s)

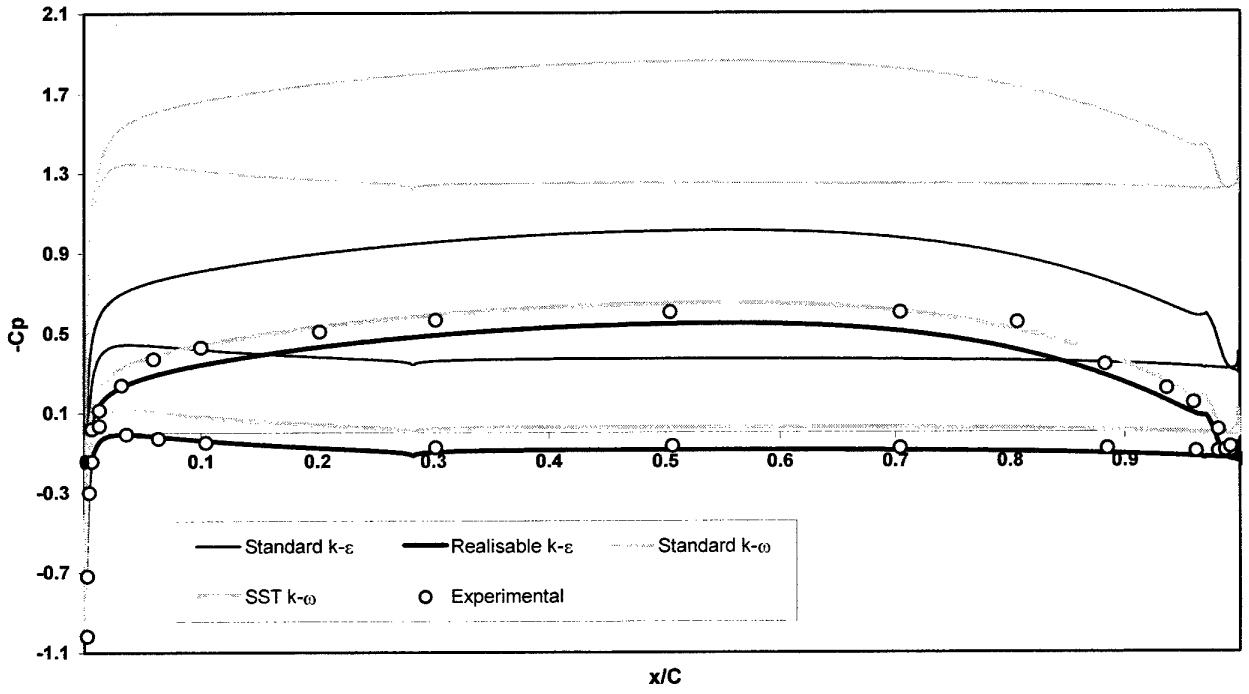

Figure 4. Turbulence Model Performance: Pressure coefficient (C_P) distribution at the surface of the hydrofoil (U_∞ = 3m/s)

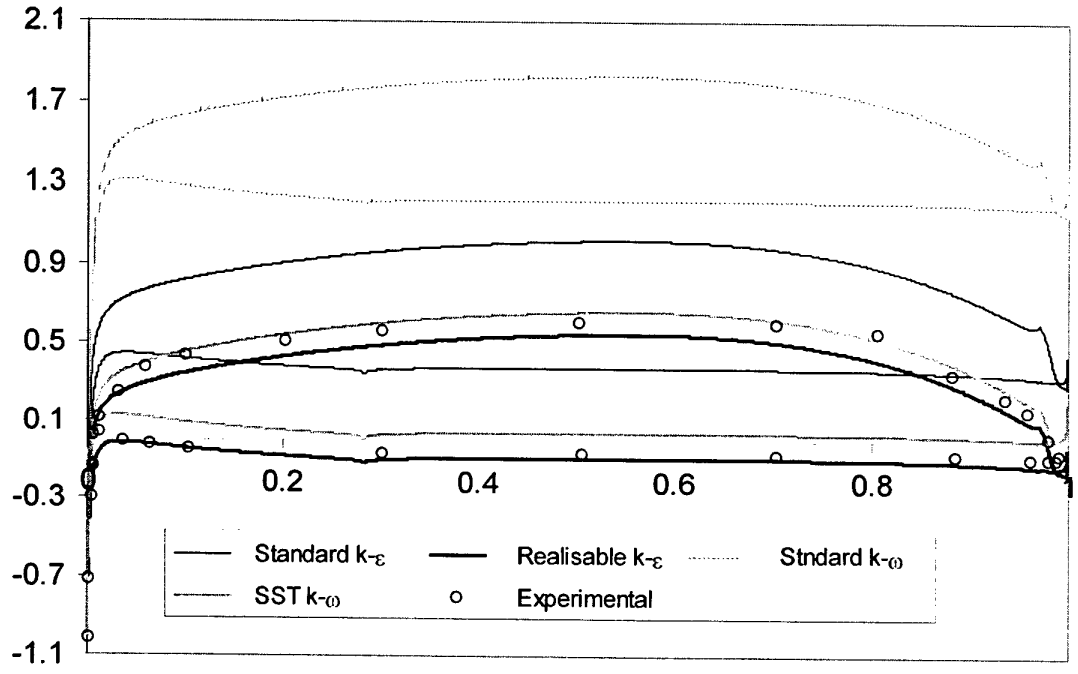

Figure 5. Turbulence Model Performance: Pressure coefficient (C_P) distribution at the surface of the hydrofoil (U_∞ = 6m/s)

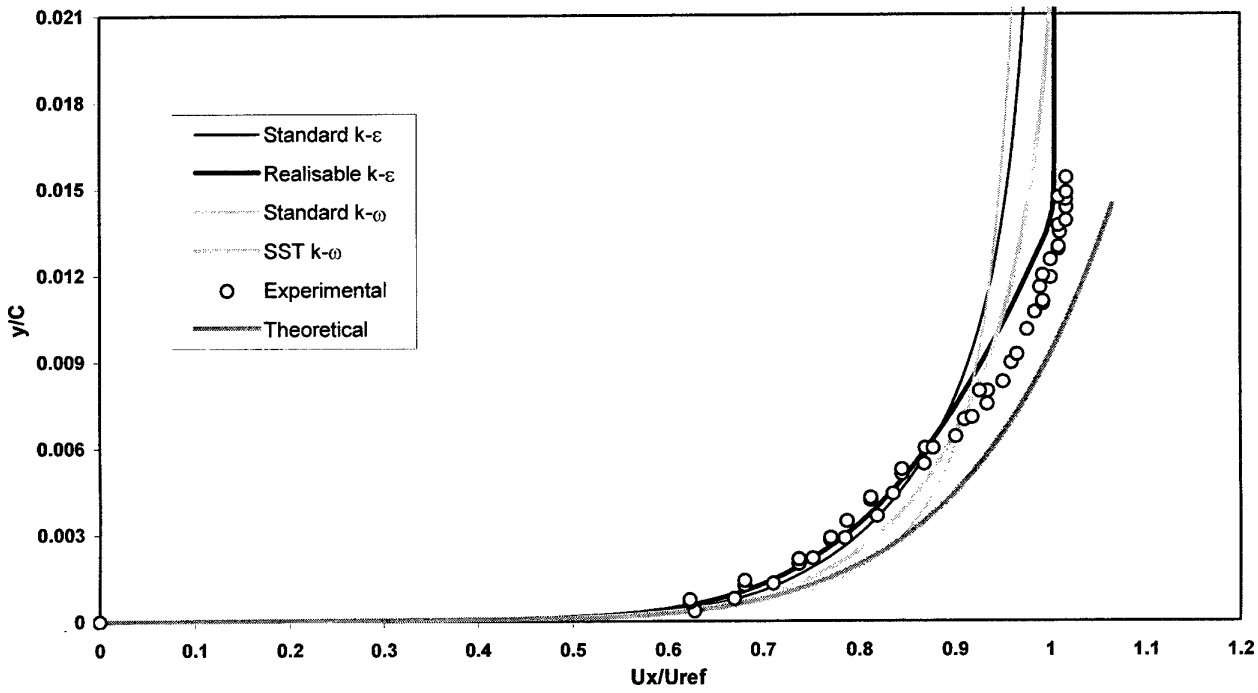

Figure 6. Turbulence Model Performance: Pressure surface boundary layer normalised mean velocity profile at 93%C (U_∞ = 3m/s)

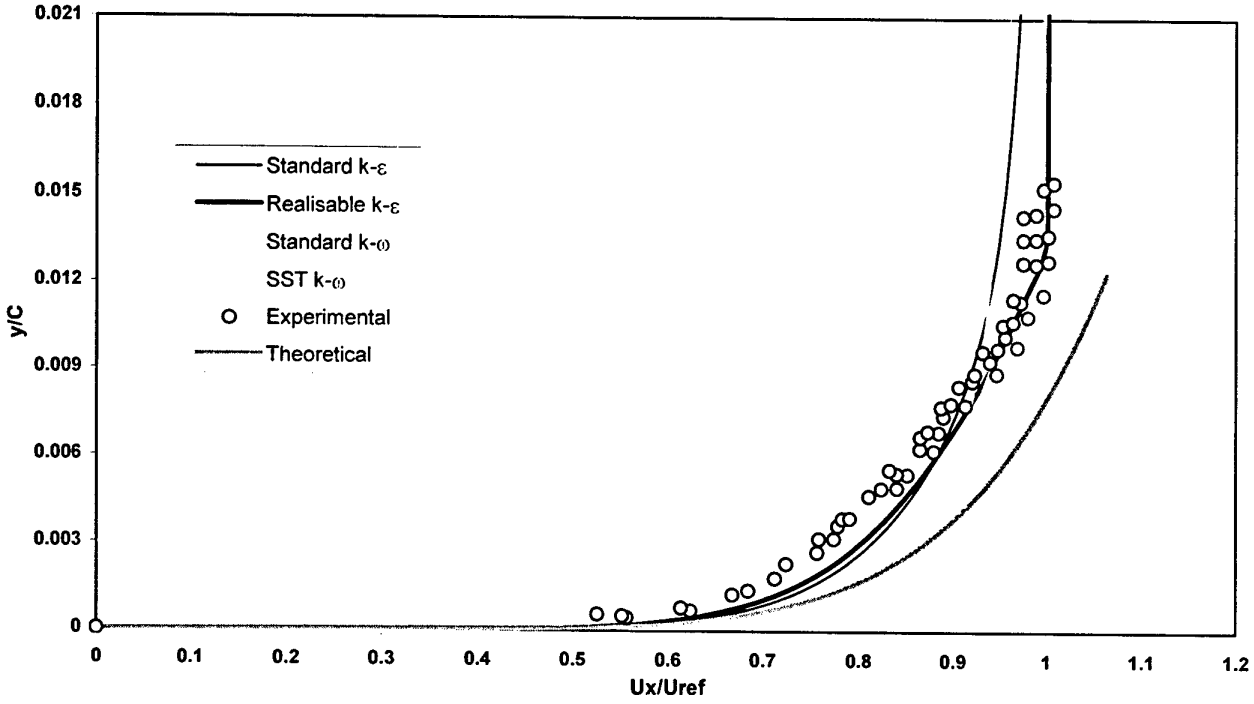

Figure 7. Turbulence Model Performance: Pressure surface boundary layer normalised mean velocity profile at 93%C (U_∞ = 6m/s)

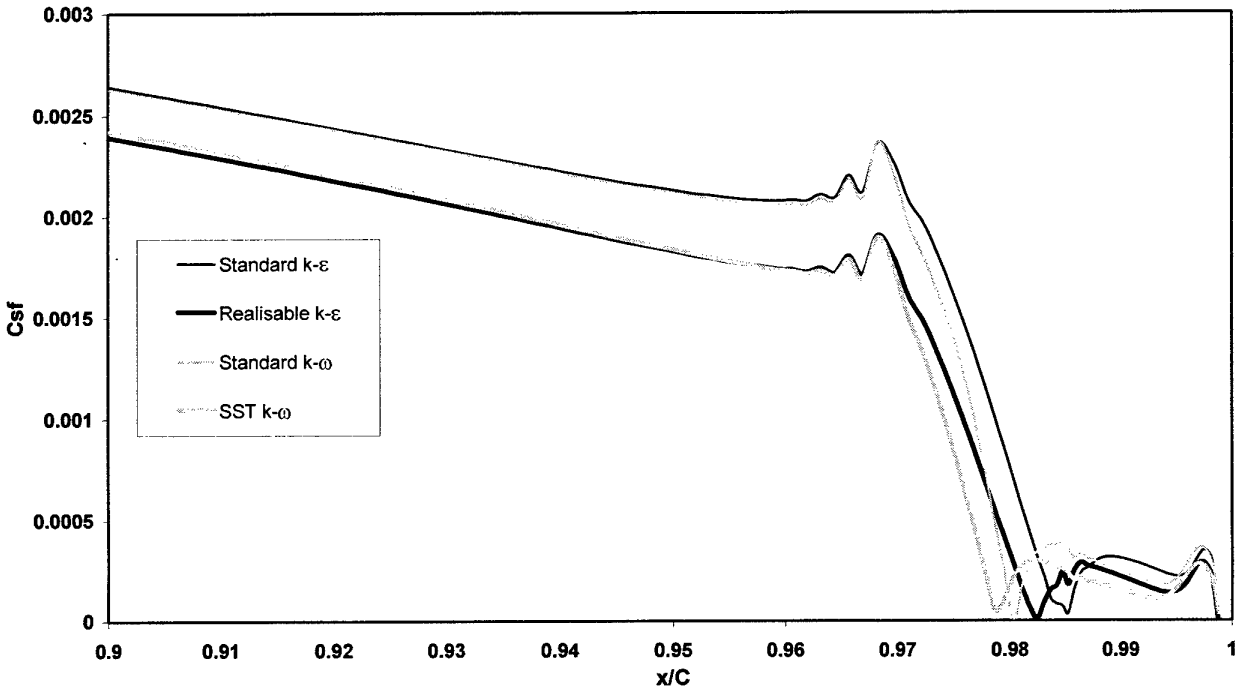

Figure 8. Turbulence Model Performance: Skin-friction coefficient distribution on the suction surface at the trailing edge (U_∞ = 3m/s)

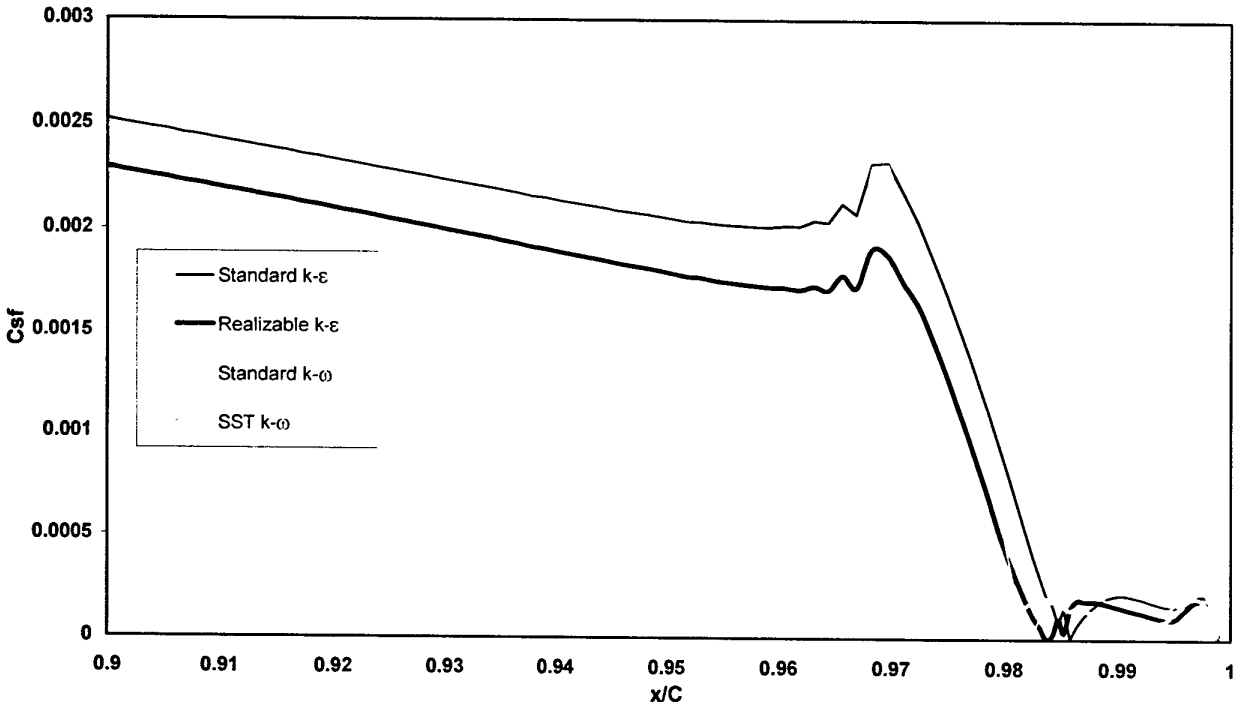

Figure 9. Turbulence Model Performance: Skin-friction coefficient distribution on the suction surface at the trailing edge (U_∞ = 6m/s)

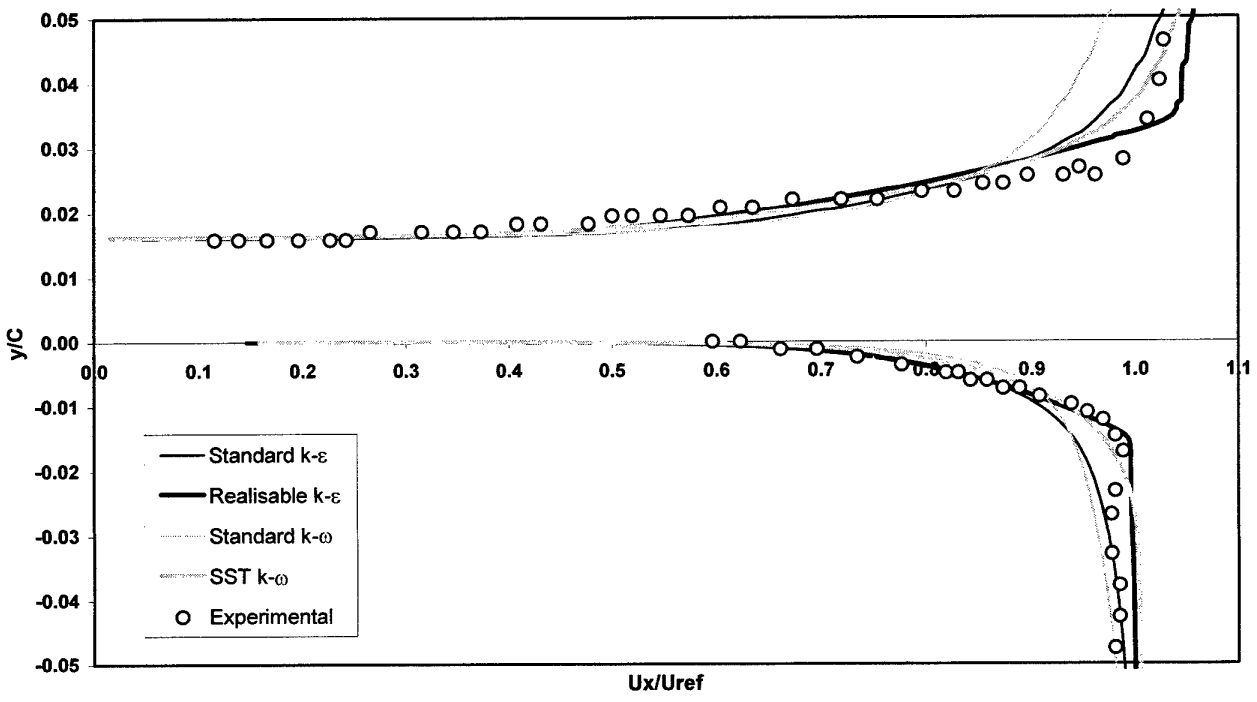

Figure 10. Turbulence Model Performance: Normalised stream-wise mean velocity profile at 97.8%C (U_∞ = 3m/s)

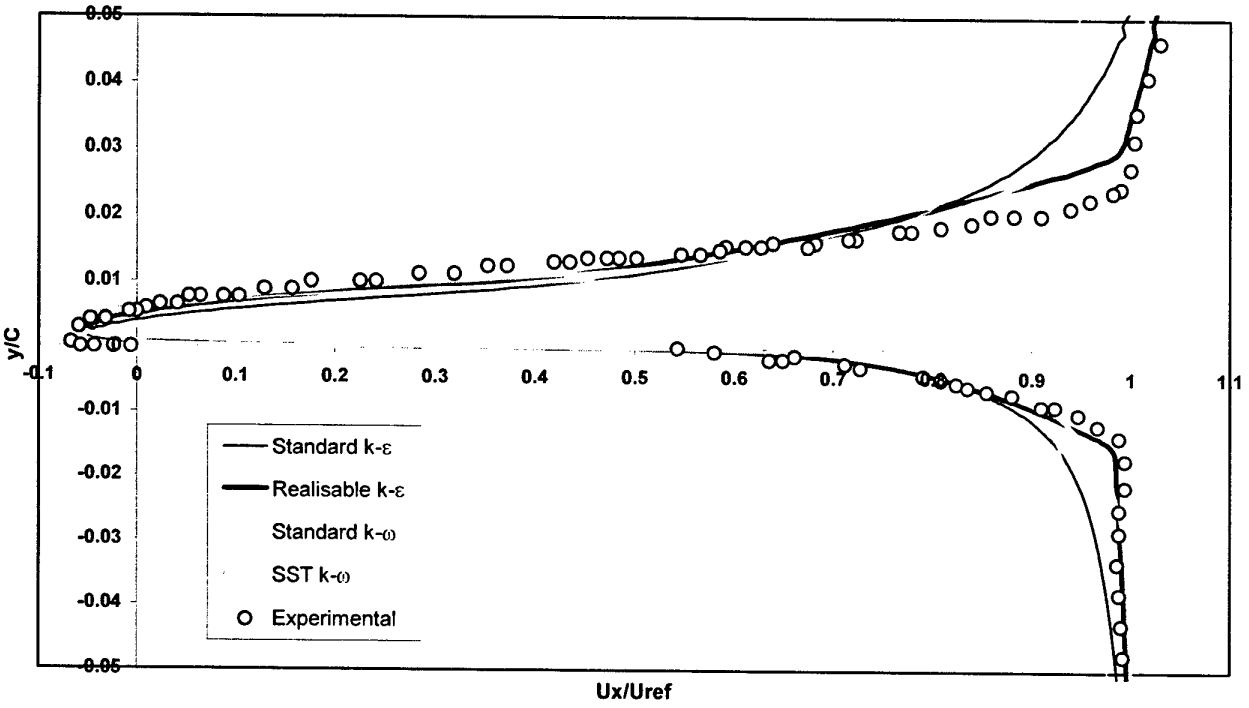

Figure 11. Turbulence Model Performance: Normalised stream-wise mean velocity profile at 100%C (U_∞ = 3m/s)

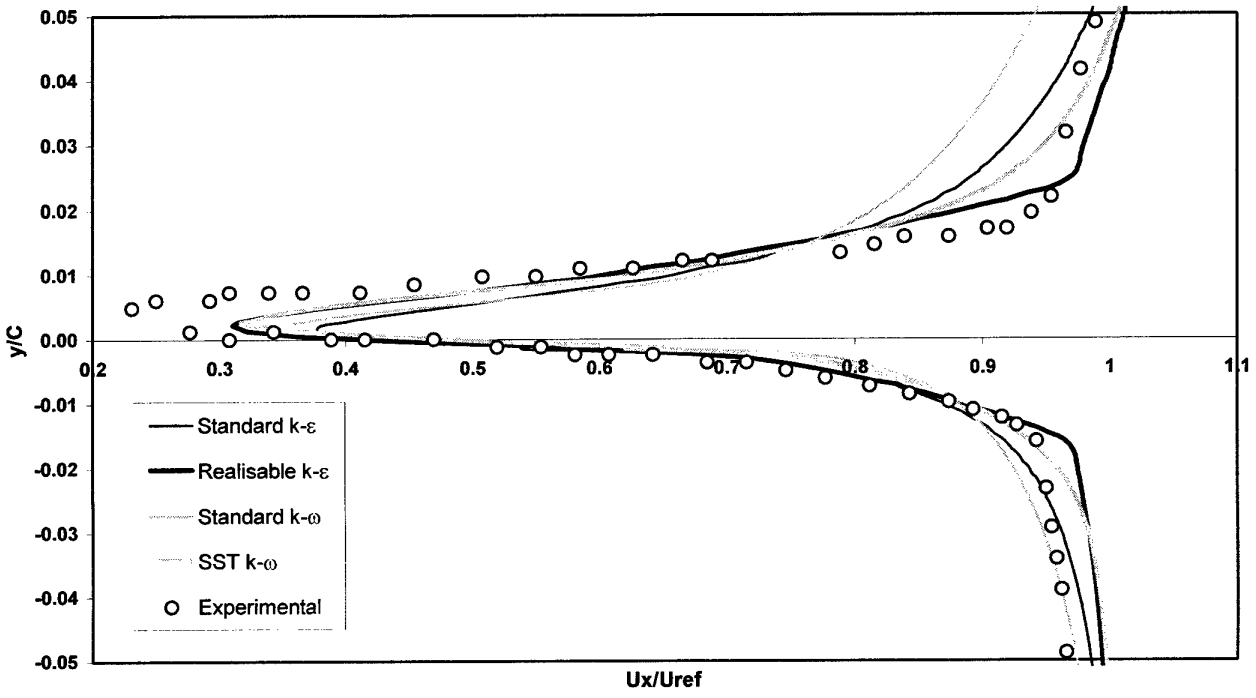

Figure 12. Turbulence Model Performance: Normalised stream-wise mean velocity profile at 102.8%C ($U_\infty = 3m/s$)

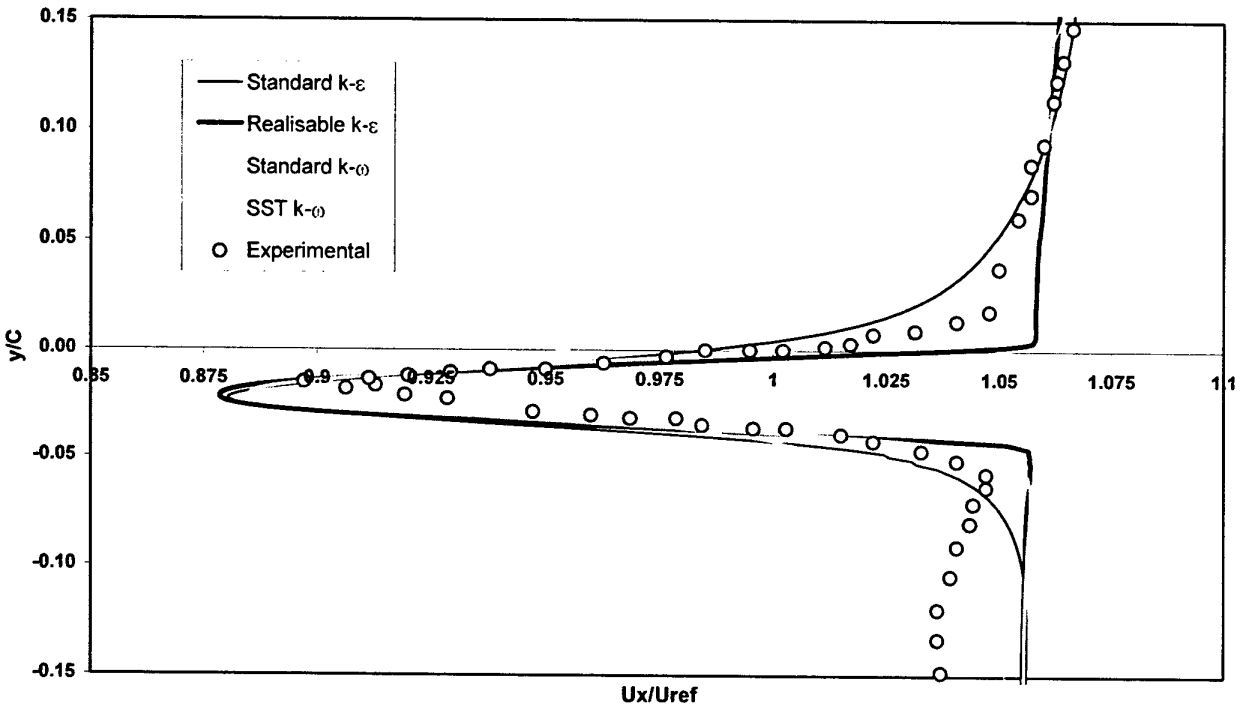

Figure 13. Turbulence Model Performance: Normalised stream-wise mean velocity profile at 150%C (U_∞ = 3m/s)

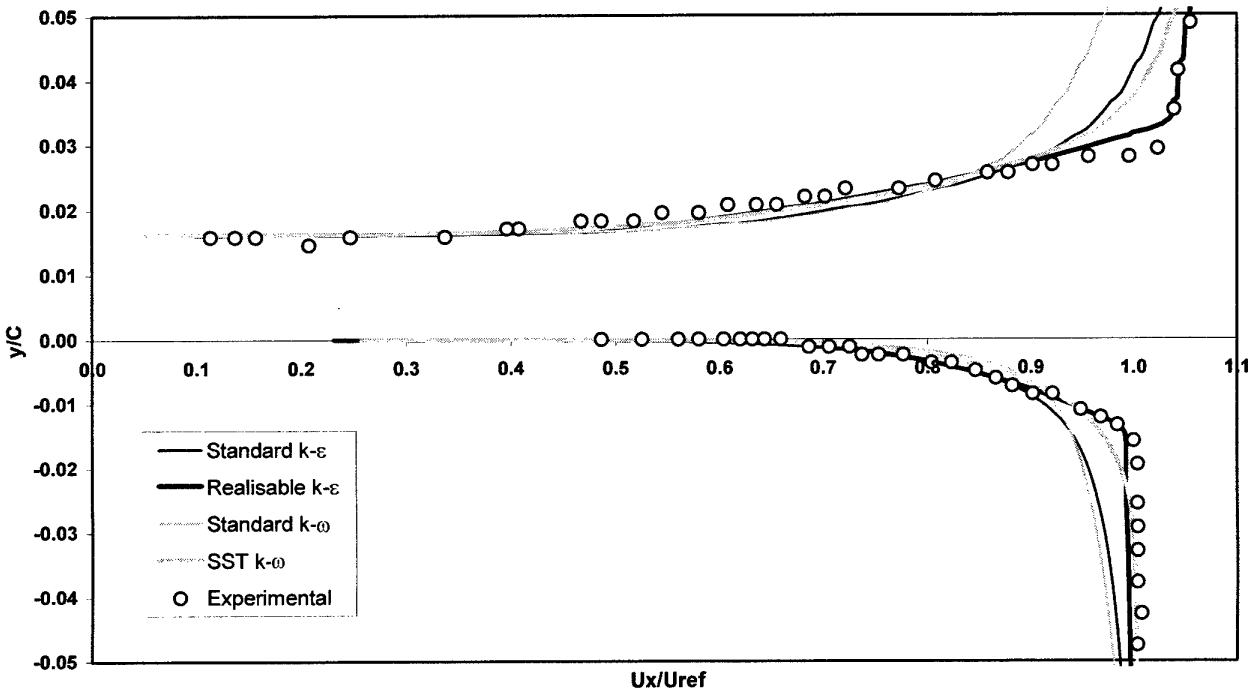

Figure 14. Turbulence Model Performance: Normalised stream-wise mean velocity profile at 97.8%C (U_∞ = 6m/s)

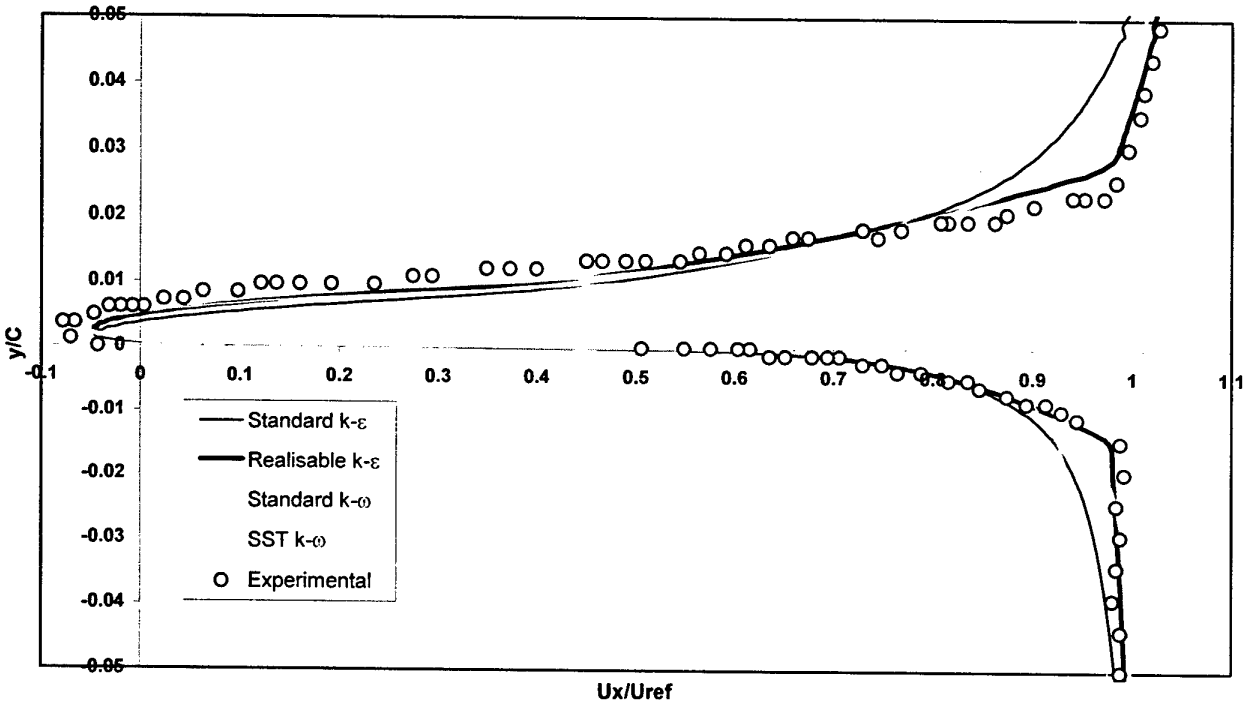

Figure 15. Turbulence Model Performance: Normalised stream-wise mean velocity profile at 100%C (U_x = 6m/s)

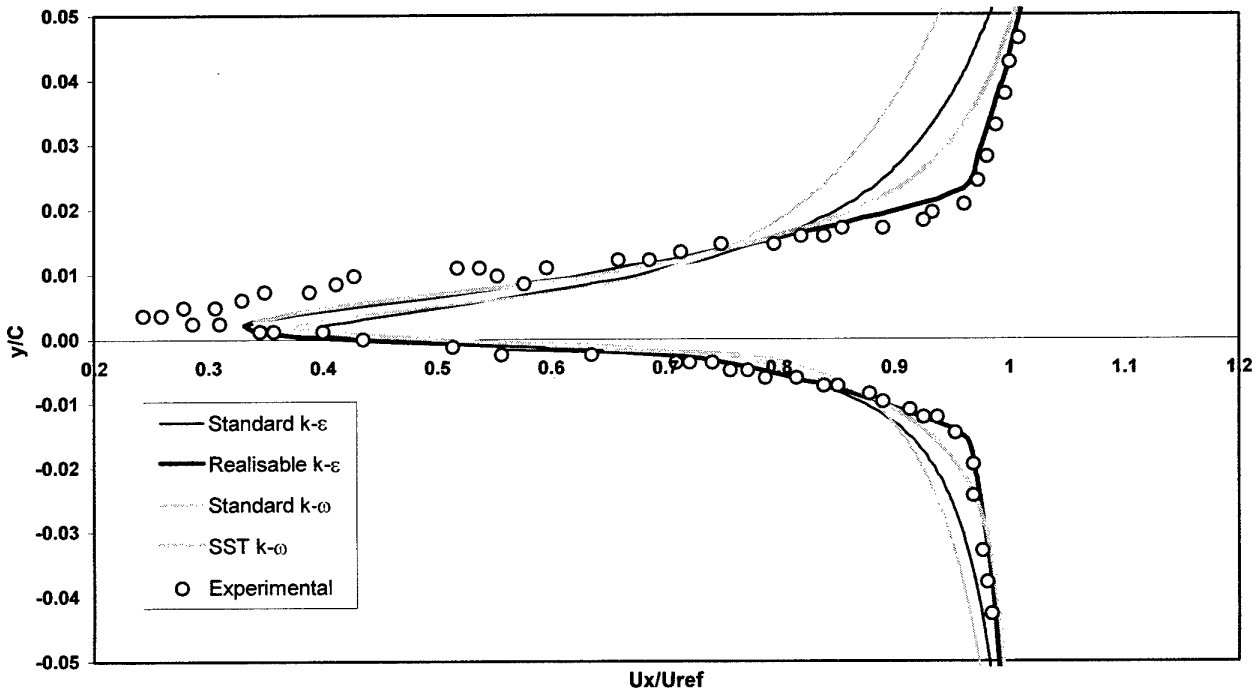

Figure 16. Turbulence Model Performance: Normalised stream-wise mean velocity profile at 102.8%C (U_∞ = 6m/s)

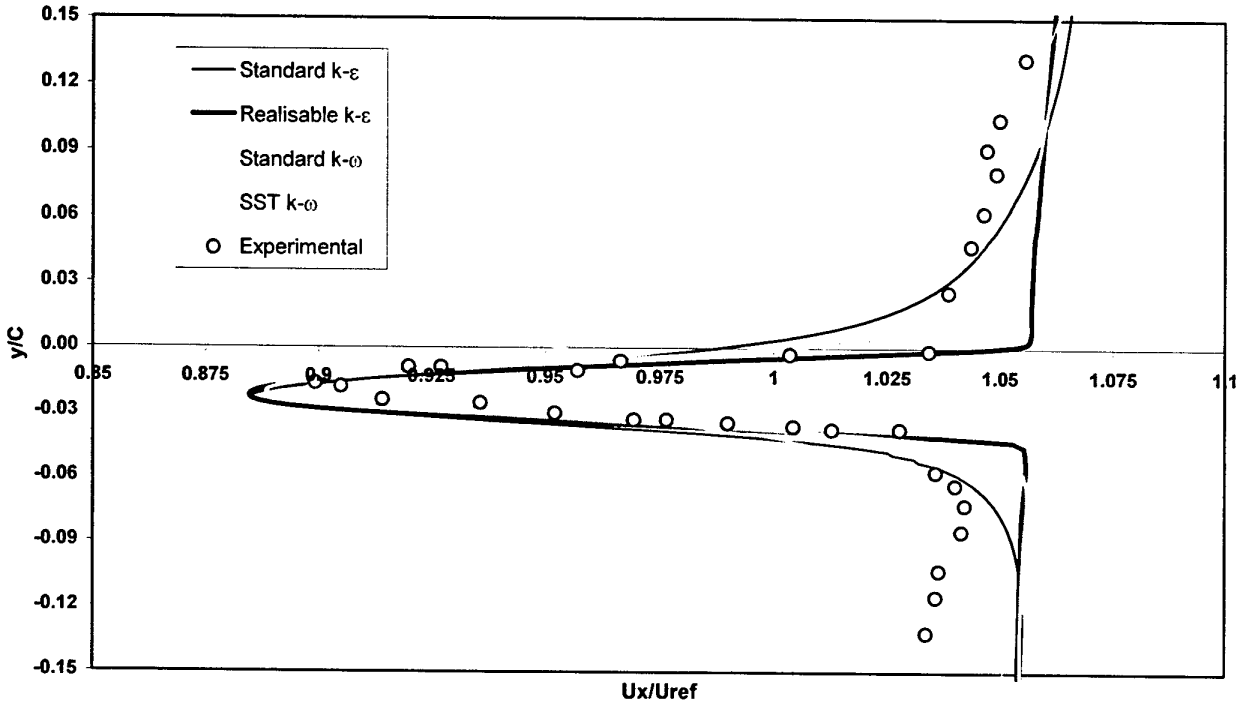

Figure 17. Turbulence Model Performance: Normalised stream-wise mean velocity profile at 150%C (U_x = 6m/s)

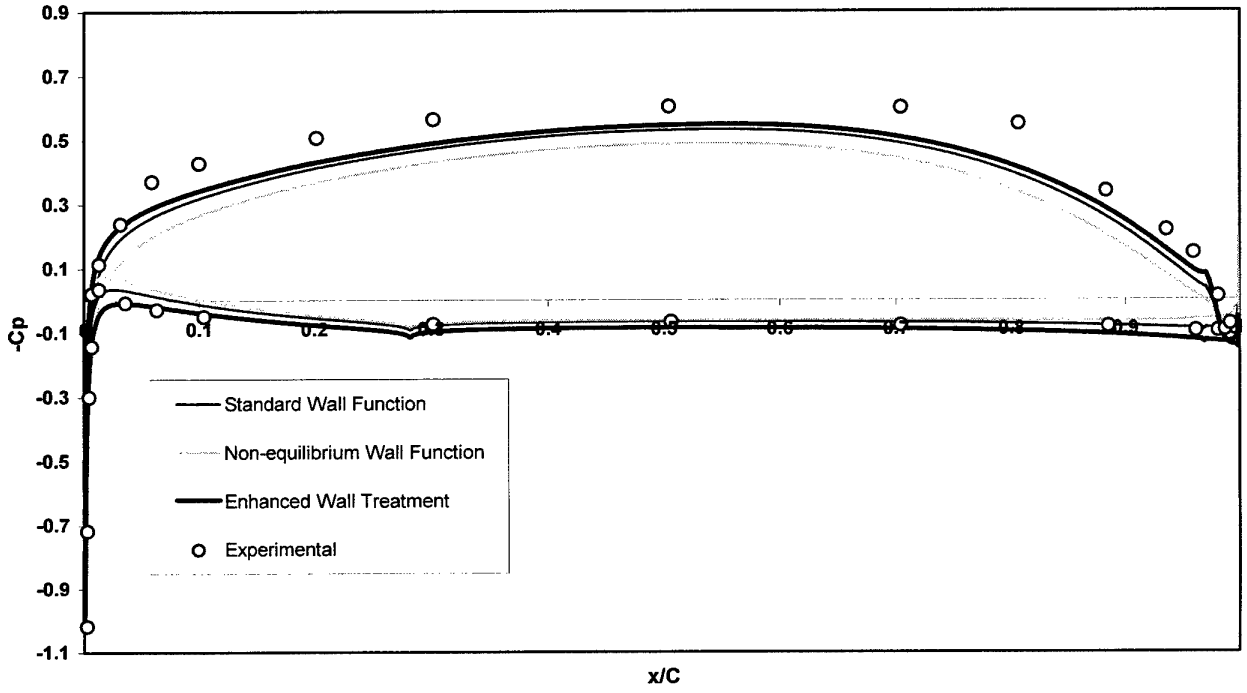

Figure 18. Wall Treatment Analysis: Pressure coefficient (C_P) distribution at the surface of the hydrofoil ($U_\infty = 3m/s$)

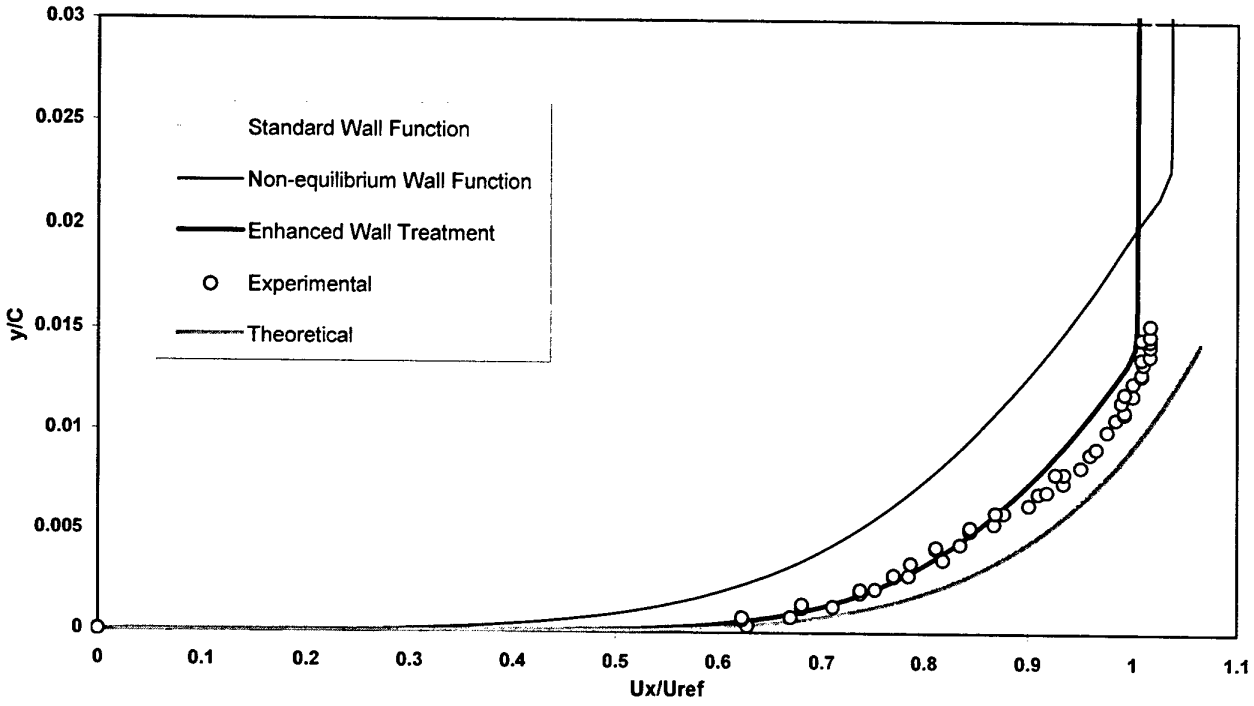

Figure 19. Wall Treatment Analysis: Pressure surface boundary layer normalised mean velocity profile at 93%C (U_∞ = 3m/s)

Table 1. Grid Independence Analysis - Mesh node and y^+ characteristics

	Nodes	*Surface Nodes*	*Maximum y^+*	*Minimum y^+*	*Average y^+*
Mesh A	42,282	570	220.11	3.37	104.35
Mesh B	98,704	1060	31.05	0.44	14.30
Mesh C	208,416	1590	4.06	0.09	2.31
Mesh D	244,026	1590	1.22	0.01	0.68

Table 2. Grid Independence Analysis – Pressure-derived Lift and Drag coefficients

	Lift coefficient		*Drag coefficient*	
Experimental	0.5520		0.0027	
	Predicted	**Error**	**Predicted**	**Error**
Mesh A	0.4945	10.42%	0.0029	7.41%
Mesh B	0.5230	5.25%	0.0025	7.41%
Mesh C	0.5302	3.95%	0.0024	11.11%
Mesh D	0.5305	3.89%	0.0024	11.11%

Table 3. Turbulence Model Performance: Hydrofoil surface forces (U_∞ = 3m/s)

Surface	*Turbulence Model*			
	Standard k-ε	**Realizable k-ε**	**Standard k-ω**	**SST k-ω**
Pressure	-9.75 kN	3.09 kN	-36.23 kN	-0.24 kN
Suction	25.63 kN	12.36 kN	51.13 kN	15.30 kN
Net lift force	15.88 kN	15.45 kN	14.90 kN	15.54 kN

Table 4. Turbulence Model Performance: Hydrofoil surface forces (U_∞ = 6m/s)

Surface	*Turbulence Model*			
	Standard k-ε	**Realizable k-ε**	**Standard k-ω**	**SST k-ω**
Pressure	-38.66 kN	13.54 kN	-125.77 kN	-0.38 kN
Suction	103.28 kN	49.47 kN	186.74 kN	61.55 kN
Net lift force	64.62 kN	63.01 kN	60.97 kN	61.93 kN

Table 5. Turbulence Model Performance: Pressure-derived Lift and Drag coefficients ($U_\infty = 3m/s$)

	Lift coefficient		***Drag coefficient***	
Experimental	0.5520		0.0027	
	Predicted	**Error**	**Predicted**	**Error**
Standard k-ε	0.5447	1.34%	0.0063	133.33%
Realisable k-ε	0.5302	4.11%	0.0024	11.11%
Standard k-ω	0.5113	7.96%	0.0147	444.44%
SST k-ω	0.5167	6.83%	0.0033	22.22%

Table 6. Turbulence Model Performance: Pressure-derived Lift and Drag coefficient ($U_\infty = 6m/s$)

	Lift coefficient		***Drag coefficient***	
Experimental	0.5486		0.00258	
	Predicted	**Error**	**Predicted**	**Error**
Standard k-ε	0.5543	1.03%	0.0062	140.31%
Realisable k-ε	0.5405	1.48%	0.0023	10.85%
Standard k-ω	0.5230	4.89%	0.00130	403.87%
SST k-ω	0.5247	4.55%	0.0033	27.91%

Table 7. Turbulence Model Performance: Pressure surface boundary layer parameters at 93%C ($U_\infty = 3m/s$)

Parameter	***Exp.***	***Theo.***	***Numerical***			
			Standard k-ε	**Realizable k-ε**	**Standard k-ω**	**SST k-ω**
Thickness (δ)	23.62 mm	30.73 mm	78.27 mm	27.79mm	115.82mm	37.82mm
Displacement thickness (δ*)	3.75 mm	3.85 mm	4.99mm	3.86mm	4.94mm	3.58mm

Table 8. Turbulence Model Performance: Pressure surface boundary layer parameters at 93%C (U_∞ = 6m/s)

Parameter	*Exp.*	*Theo.*	*Numerical*			
			Standard k-ε	**Realizable k-ε**	**Standard k-ω**	**SST k-ω**
Thickness (δ)	24.81 mm	26.75m m	92.74mm	26.44mm	116.30mm	38.06mm
Displacement thickness (δ*)	4.44 mm	3.35mm	4.67mm	3.74mm	4.69mm	3.33mm

Table 9. Wall Treatment Analysis: Pressure-derived Lift and Drag coefficients (U_∞ = 3m/s)

	Lift coefficient		*Drag coefficient*	
Experimental	0.5520		0.0027	
	Predicted	**Error**	**Predicted**	**Error**
Standard Wall Function	0.4529	17.95%	0.0026	3.70%
Non-equilibrium Wall Function	0.3933	28.75%	0.0036	33.33%
Enhanced Wall Treatment	0.5302	4.11%	0.0024	11.11%

DISTRIBUTION LIST

Steady-State Evaluation of 'Two-Equation' RANS (Reynolds-averaged Navier-Stokes) Turbulence Models for High-Reynolds Number Hydrodynamic Flow Simulations

Nicholas J. Mulvany, Li Chen, Jiyuan Y. Tu and Brendon Anderson

AUSTRALIA

DEFENCE ORGANISATION

	No. of copies
Task Sponsor	
CAPDEV (SM)	1
S&T Program	
Chief Defence Scientist	shared copy
FAS Science Policy	
AS Science Corporate Management	
Director General Science Policy Development	
Counsellor Defence Science, London	Doc Data Sheet
Counsellor Defence Science, Washington	Doc Data Sheet
Scientific Adviser to MRDC, Thailand	Doc Data Sheet
Scientific Adviser Joint	1
Navy Scientific Adviser	1
Scientific Adviser - Army	Doc Data Sht & Dist List
Air Force Scientific Adviser	Doc Data Sht & Dist List
Scientific Adviser to the DMO M&A	Doc Data Sht & Dist List
Scientific Adviser to the DMO ELL	Doc Data Sht & Dist List
Director of Trials	1
Platforms Sciences Laboratory	
Chief of Maritime Platforms Division	Doc Data Sht & Dist List
Research Leader: Janis Cocking	Doc Data Sht & Dist List
Brendon Anderson	5
Li Chen	1
DSTO Library and Archives	
Library Fishermans Bend	Doc Data Sheet
Library Edinburgh	1
Australian Archives	1
Capability Systems Division	
Director General Maritime Development	Doc Data Sheet
Director General Aerospace Development	Doc Data Sheet
Director General Information Capability Development	Doc Data Sheet
Office of the Chief Information Officer	

Deputy CIO — Doc Data Sheet
Director General Information Policy and Plans — Doc Data Sheet
AS Information Structures and Futures — Doc Data Sheet
AS Information Architecture and Management — Doc Data Sheet
Director General Australian Defence Simulation Office — Doc Data Sheet

Strategy Group

Director General Military Strategy — Doc Data Sheet
Director General Preparedness — Doc Data Sheet

HQAST

SO (Science) (ASJIC) — Doc Data Sheet

Navy

SO (SCIENCE), COMAUSNAVSURFGRP, NSW — Doc Data Sht & Dist List
Director General Navy Capability, Performance and Plans, Navy Headquarters — Doc Data Sheet
Director General Navy Strategic Policy and Futures, Navy Headquarters — Doc Data Sheet
COMAUSNAVSYSCOM — 1

Army

ABCA National Standardisation Officer, Land Warfare Development Sector, Puckapunyal — e-mailed Doc Data Sheet
SO (Science), Deployable Joint Force Headquarters (DJFHQ) (L), Enoggera QLD — Doc Data Sheet
SO (Science) - Land Headquarters (LHQ), Victoria Barracks NSW — Doc Data & Exec Summ

Intelligence Program

DGSTA Defence Intelligence Organisation — 1
Manager, Information Centre, Defence Intelligence Organisation — 1 + pdf version
Assistant Secretary Corporate, Defence Imagery and Geospatial Organisation — Doc Data Sheet

Defence Materiel Organisation

Head Airborne Surveillance and Control — Doc Data Sheet
Head Aerospace Systems Division — Doc Data Sheet
Head Electronic Systems Division — Doc Data Sheet
Head Maritime Systems Division — Doc Data Sheet
Head Land Systems Division — Doc Data Sheet
Head Industry Division — Doc Data Sheet
Chief Joint Logistics Command — Doc Data Sheet
Management Information Systems Division — Doc Data Sheet
Head Materiel Finance — Doc Data Sheet

Defence Libraries

Library Manager, DLS-Canberra — Doc Data Sheet
Library Manager, DLS - Sydney West — Doc Data Sheet

OTHER ORGANISATIONS

National Library of Australia	1
NASA (Canberra)	1

UNIVERSITIES AND COLLEGES

Australian Defence Force Academy	
Library	1
Head of Aerospace and Mechanical Engineering	1
Serials Section (M list), Deakin University Library, Geelong, VIC	1
Hargrave Library, Monash University	Doc Data Sheet
Librarian, Flinders University	1

OUTSIDE AUSTRALIA

INTERNATIONAL DEFENCE INFORMATION CENTRES

US Defense Technical Information Center	2
UK Defence Research Information Centre	2
Canada Defence Scientific Information Service	e-mail link to pdf
NZ Defence Information Centre	1

ABSTRACTING AND INFORMATION ORGANISATIONS

Library, Chemical Abstracts Reference Service	1
Engineering Societies Library, US	1
Materials Information, Cambridge Scientific Abstracts, US	1
Documents Librarian, The Center for Research Libraries, US	1

SPARES	5
Total number of copies:	**36**

DEFENCE SCIENCE AND TECHNOLOGY ORGANISATION
DOCUMENT CONTROL DATA

1. PRIVACY MARKING/CAVEAT (OF DOCUMENT)

2. TITLE

Steady-State Evaluation of 'Two-Equation' RANS (Reynolds-averaged Navier-Stokes) Turbulence Models for High-Reynolds Number Hydrodynamic Flow Simulations

3. SECURITY CLASSIFICATION (FOR UNCLASSIFIED REPORTS THAT ARE LIMITED RELEASE USE (L) NEXT TO DOCUMENT CLASSIFICATION)

Document	(U)
Title	(U)
Abstract	(U)

4. AUTHOR(S)

Nicholas J. Mulvany, Li Chen, Jiyuan Y. Tu and Brendon Anderson

5. CORPORATE AUTHOR

Platform Sciences Laboratory
506 Lorimer St.
Fishermans Bend, Victoria, 3207
Australia

6a. DSTO NUMBER	6b. AR NUMBER	6c. TYPE OF REPORT	7. DOCUMENT DATE
DSTO-TR-1564	AR-013-055	Technical Report	March 2004

8. FILE NUMBER	9. TASK NUMBER	10. TASK SPONSOR	11. NO. OF PAGES	12. NO. OF REFERENCES
2003/10150	NAV 03/136	COMAUSNAVSUB GRP	54	21

13. URL on the World Wide Web

http://www.dsto.defence.gov.au/corporate/reports/DSTO-TR-1564.pdf

14. RELEASE AUTHORITY

Chief, Maritime Platforms Division

15. SECONDARY RELEASE STATEMENT OF THIS DOCUMENT

Approved for public release

OVERSEAS ENQUIRIES OUTSIDE STATED LIMITATIONS SHOULD BE REFERRED THROUGH DOCUMENT EXCHANGE, PO BOX 1500, EDINBURGH, SA 5111

16. DELIBERATE ANNOUNCEMENT

No Limitations

17. CITATION IN OTHER DOCUMENTS Yes

18. DEFTEST DESCRIPTORS

Turbulence modelling, RANS, Computational fluid, Dynamics, CFD, Hydrofoil, High Reynolds number, Boundary layer separation

19. ABSTRACT

This report presents an evaluation of the steady-state capability of the turbulence models available in the commercial CFD code FLUENT 6.0, for their application to the simulation of hydrofoil turbulent boundary layer separation at high-Reynolds numbers. Four widely applied two-equation RANS turbulence models were qualitatively and quantitatively assessed through comparison with high-quality experimental data at Reynolds numbers of 8.284´106 and 1.657´107. The turbulence models evaluated were the Standard k-e model, the Realisable k-e model, the Standard k-w model and the Shear-Stress-Transport (SST) k-w model. It was concluded that the Realisable k-e turbulence model used with enhanced wall functions and near-wall modelling techniques, consistently provided superior performance in predicting the hydrofoil's performance parameters and flow characteristics.